Undercompressive Shocks in Thin Film Flows

A. L. Bertozzi [a], A. Münch [a], and M. Shearer [b]

[a] *Department of Mathematics, Duke University, Durham, NC 27708,*
bertozzi@math.duke.edu, amue@math.duke.edu

[b] *Department of Mathematics and Center for Research in Scientific Computation, North Carolina State University, Raleigh, NC 27695-8205,*
shearer@math.ncsu.edu

Abstract

Equations of the type

$$h_t + (h^2 - h^3)_x = -\epsilon^3 (h^3 h_{xxx})_x$$

arise in the context of thin liquid films driven by the competing effects of a thermally induced surface tension gradient and gravity. In this paper, we focus on the interaction between the fourth order regularization and the nonconvex flux. Jump initial data, from a moderately thick film to a thin precurser layer, is shown to give rise to a double wave structure that includes an undercompressive wave. This wave, which approaches an undercompressive shock as $\epsilon \to 0$, is an accumulation point for a countable family of compressive waves having the same speed. The family appears through a series of bifurcations parameterized by the shock speed. At each bifurcation, a pair of traveling waves is produced, one being stable for the PDE, the other unstable. The conclusions are based primarily on numerical results for the PDE, and on numerical investigations of the ODE describing traveling waves. Fourth order *linear* regularization is observed to produce a similar bifurcation structure of traveling waves.

Key words: undercompressive shock, capillarity, thin films, Marangoni stress, fourth order diffusion, numerical simulation, hyperbolic conservation law

Contents

1 Introduction

Consider the motion of a thin liquid film on an inclined planar surface, driven by competing effects of gravity and a thermally induced surface tension gradient. This problem has been the focus of experimental investigation [10,39]; it is important in understanding the dynamics of a variety of industrial coating processes such as the formation and protection of microchips, de-icing of airplane wings and the construction of photographic film. Related problems concerning the dynamics of thin films have been the subject of much recent mathematical research (see [7] and references therein).

In this paper, we model the thin film motion by a partial differential equation for the thickness $h(x,t)$ of the film above the inclined plane, as a function of distance x down the plane, and time t. (While dependence on an additional, transverse, spatial variable y is important, in this paper, we take h to be independent of y.) The PDE model takes the form

$$h_t + (h^2 - \alpha h^3)_x = \beta(h^3 h_x)_x - \gamma(h^3 h_{xxx})_x, \tag{1}$$

in which the nonnegative parameters α, β, γ contain effects of surface tension, gravity and the slope of the plane.

The main results of the paper concern the case $\beta = 0$, corresponding physically to a vertical plane; small β, corresponding to a nearly vertical plane or a flow in which the thermally induced surface tension gradient is dominated by the combined effects of surface tension and gravity, has qualitatively the same behavior as the case $\beta = 0$. Mathematically, taking $\beta = 0$ allows us to focus on the interplay between the nonconvex nonlinearity in the convective term, and the fourth order diffusion, without the complication of the second order diffusion. This interaction introduces wave propagation phenomena that are strikingly new, both for the application to thin films, and for the theory of traveling wave approximations to shock waves.

After a suitable rescaling, the case $\beta = 0$ leads to the equation

$$h_t + (h^2 - h^3)_x = -\epsilon^3(h^3 h_{xxx})_x, \tag{2}$$

in which $\epsilon > 0$ is a small parameter. Traveling wave solutions, referred to in this paper as *capillary shock profiles,* steepen as $\epsilon \to 0$ to shock wave solutions of the scalar conservation law

$$h_t + (h^2 - h^3)_x = 0. \tag{3}$$

The traveling waves connect an upstream height h_∞ to a (small) downstream height $b < h_\infty$.

When $h_\infty - b$ is small, the traveling wave is *compressive* in the sense that characteristics for equation (3) approach each other from either end of the wave:

$$\lambda(h_\infty) > s > \lambda(b), \tag{4}$$

where s is the speed of the traveling wave, and $\lambda(h) = 2h - 3h^2$ is the characteristic speed. The corresponding shock wave satisfying (4) is called a *Lax shock*; inequalities (4) constitute the Lax entropy condition [37] for discontinuous solutions of the scalar conservation law (3).

As h_∞ increases, we find there are multiple traveling waves approximating the Lax shock. Some of these are asymptotically stable for equation (2), others unstable. In this range of h_∞ we find a further stable solution of the equation (2) composed of two waves traveling with different speeds. The slower wave corresponds to a Lax shock joining h_∞ to a height $h_{uc} > h_\infty$, independent of h_∞, so that the shock strength decreases with increasing h_∞; the faster wave corresponds to an *undercompressive* shock from h_{uc} to b. The latter wave is undercompressive in the sense that it violates the Lax condition; characteristics pass through the shock instead of impinging on it:

$$\max(\lambda(h_{uc}), \lambda(b)) < s_{uc}, \tag{5}$$

where s_{uc} denotes the speed of the undercompressive wave.

For still larger values of h_∞, there are no compressive traveling waves joining h_∞ to b, and although the double shock wave structure persists for $h_\infty < h_{uc}$, it gives way for $h_\infty > h_{uc}$ to a two wave structure in which the slower wave is a rarefaction wave solution of (3).

Undercompressive shock waves for scalar conservation laws have been studied in contexts in which they are approximated by traveling wave solutions of equations that include *second order* dissipation and dispersion, in contrast to the fourth order non-dispersive equation of this paper [23,24,29]. Undercompressive shocks, together with other types of non-classical shocks, have been studied in various applications involving systems of equations [1,28,43,45,47].

The dynamics of the undercompressive double shock structure has been observed in a recent experiment [17] in which silicon oil (PDMS) is driven up an inclined oxidized silicon wafer by a thermal gradient. In previous experimental studies of very thin films ($h_\infty << 1$) [10], the speed of the front agrees extremely well with that predicted by the classical theory involving only Lax shocks. In the experiments of [17] however, with films of intermediate thickness, gravity plays a larger role. It has been observed that for these thicker films, the front speed is effectively independent of the film thickness h_∞, an observation consistent with the formation of an undercompressive shock as the leading front. Moreover, the thickness profile of the film compares very well with the shape of the film observed in numerical simulations of (1) of the double shock structure [4]. (The experimental measurements are taken at times just before the shocks are predicted by

the theory to completely separate.)

A further remarkable observation in this experiment is that the front forms an extremely large capillary ridge that tends to remain stable, in contrast to all other driven film experiments in which a capillary ridge is observed to break up into rivulets [11,27,30,44]. The undercompressive shock is believed to play a role in preventing the contact line from fingering in this way. To the best of our knowledge, this recent experiment is the first documented observation of an undercompressive shock in an application modeled by a scalar conservation law.

The paper is organized as follows. In Section 2, we review the physical problem, derive a model partial differential equation, and nondimensionalize using scales that highlight the role of fourth order diffusion. In Section 3, we review Lax shocks and rarefaction waves for equation (3). Also in this section, we discuss traveling wave solutions for Lax shocks for equation (1), both in the straightforward case $\gamma = 0$ of (nonlinear) second order diffusion, and in the case of fourth order diffusion $\beta = 0$, but with a convex nonlinear flux transport ($\alpha = 0$). Traveling waves in the latter case are established using arguments of ([41,42]). In Section 4, we present the main numerical results for equation (2), illustrating that there is a transition from weak Lax shocks to the undercompressive double shock structure as the film thickness is increased. In Section 5, we discuss traveling waves for (2) directly. This involves the study of a family of ordinary differential equations with parameters depending on h_∞ and b. Here, we examine the existence of the undercompressive shock, and the associated cascade of bifurcations giving rise to the multiple compressive traveling waves for the same Lax shock. In Section 6, we show that for larger b near $1/3$, the bifurcation structure of the traveling waves can be understood by studying a simpler equation, derived by expanding around $h = \frac{1}{3}$; The simpler equation has a cubic nonlinearity and linear fourth order diffusion. Numerical results for this equation are similar to those for the full equation, and show that the complex dynamics introduced in Sections 4 and 5 is really due to the fourth order operator on the right hand size of (2) as opposed to the nonlinear diffusion. In Section 7, we derive a priori bounds for the values of h in a traveling wave, using two techniques. In the final section, we draw attention to various issues related to the numerical study in this paper. Among these are the stability of the computed one-dimensional fronts to two-dimensional perturbations, the effect of second order diffusive terms on the dynamics and the singular limit as $b \to 0$. We also propose some open analysis problems motivated by the numerical work here.

2 The model

We consider the dynamics of a thin layer of liquid of thickness h on an inclined surface driven by thermally created surface tension gradients and influenced by gravity (see Fig. 1). Let τ denote the surface tension gradient, α the angle (from horizontal) of inclination of the plane, ρ the density of the liquid, g the gravitational constant, η the dynamic viscosity of the liquid, and γ the surface tension of the liquid. The spatial

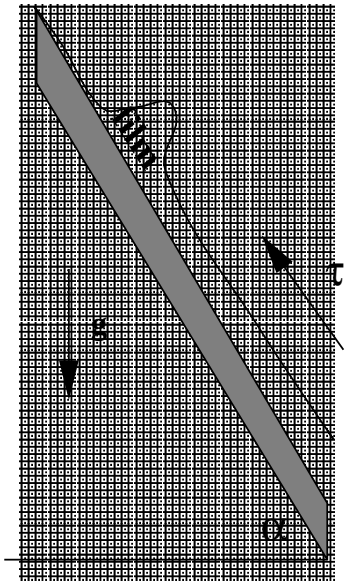

Fig. 1. A schematic diagram of the physical problem. A thin film of viscous liquid flows up an inclined plane due to Marangoni stresses created by a temperature gradient on the plane. Gravity works against the stress to drive fluid back down the plane.

variables x and y denote respectively the direction of the flow and the direction normal to the flow, both in the plane parallel to the incline.

Conservation of mass of the liquid requires that

$$h_t + \nabla \cdot (h\vec{V}) = 0, \tag{6}$$

where V is a 'depth averaged' velocity of the liquid. The formula for V we use is from [9,16] in which a lubrication approximation gives

$$\vec{V} = (\frac{\tau h}{2\eta} - \frac{\rho g h^2 \sin\alpha}{3\eta})\vec{e}_x - \frac{\rho g h^2 \cos\alpha}{3\eta}\nabla h + \frac{\gamma h^2 \nabla^3 h}{3\eta}. \tag{7}$$

The coefficient of $\vec{e}_x$ in the expression for $\vec{V}$ represents convection of the film due to a surface tension gradient and due to the component of gravity tangent to the surface. The ∇h represents diffusion of the liquid due to the normal component of gravity while the last term represents diffusion of the liquid due to surface tension.

For the purpose of this paper, we ignore the dependence of the solution on the direction transverse to the flow, i.e. we consider solutions h depending only on x and t:

$$h_t + (f(h))_x = -(\frac{\gamma h^3 h_{xxx}}{3\eta})_x + (\frac{\cos\alpha \rho g h^3}{3\eta} h_x)_x, \tag{8}$$

where

$$f(h) = \frac{\tau h^2}{2\eta} - \frac{\sin\alpha \rho g h^3}{3\eta}.$$

To nondimensionalize the equation, we introduce length scales H, l, and a corresponding

time scale T:

$$h = H\hat{h}, \quad x = \hat{x}l, \quad \text{and} \quad t = T\hat{t}. \tag{9}$$

Balancing the competing convective effects of gravity and Marangoni forces in $f(h)$ gives

$$H = \frac{3\tau}{2\sin\alpha\rho g}.$$

Setting l to be the capillary length on which surface tension balances the driving forces on the right hand side of (8) gives

$$l = (\frac{2\gamma}{3\tau H^2})^{1/3} = (\frac{3\gamma\tau}{2\rho^2 g^2 \sin^2\alpha})^{1/3}.$$

The time scale is then chosen to be the one on which all three of these effects balance,

$$T = 2\frac{\eta}{\tau^2}(\frac{4}{9}\tau\gamma\rho g\sin\alpha)^{1/3}.$$

The end result (removing the $\hat{}$ from the variables in (9)) is a rescaled dimensionless equation of the form

$$\boxed{h_t + (h^2 - h^3)_x = -(h^3 h_{xxx})_x + D(h^3 h_x)_x} \tag{10}$$

where

$$D = (\frac{9}{4}\frac{\tau^2}{\gamma\rho g})^{1/3}\frac{\cot\alpha}{(\sin\alpha)^{1/3}}\ . \tag{11}$$

We are interested in studying the structure of traveling wave solutions of (10). For the physical problem described above, we expect to have a situation where there is a front of fluid that connects to a constant height upstream,

$$h \to h_\infty \quad \text{as} \quad x \to -\infty.$$

Although the physical problem has a contact line downstream, as suggested by Fig. 1, we choose the boundary condition

$$h \to b > 0 \quad \text{as} \quad x \to \infty.$$

Such a boundary condition is necessary for the model (7) since it is based on the assumption of a 'no-slip' boundary condition which results in a well-known paradox [14,26] for the case of a moving contact line. To remove the singularity, we consider the same 'precursor model' used in [46] for flow down an inclined plane (see also ([3,33]).

In the experiments studied so far [4,10,16,17] the effect of gravity normal to the surface is small compared with the other effects, and the slope of the film is small compared to

the slope of the incline. In all of these studies, the dimensionless parameter D is less than $\frac{1}{2}$ and the problem is well approximated by the model equation with $D = 0$. Thus, we set $D = 0$ for the remainder of the paper however we make some comments and conjectures throughout regarding the dynamics when D is larger.

The length scale (in x) over which h transitions from h_∞ to b in a traveling wave or shock layer is order one in the formulation (10) above. We can think of this traveling wave as a viscous regularization of a shock wave, if we let $x' = x\epsilon$ and $t' = \epsilon t$, so that (10) becomes

$$h_{t'} + (h^2 - h^3)_{x'} = -\epsilon^3 (h^3 h_{x'x'x'})_{x'}. \tag{12}$$

This equation is a fourth order nonlinear singular perturbation of the conservation law

$$h_{t'} + (h^2 - h^3)_{x'} = 0 \tag{13}$$

which has a non-convex flux function $f(h) = h^2 - h^3$. As we show in later sections, the dynamics of (12) for small ϵ is significantly different from the dynamics of (13) in the vanishing viscosity limit with lower order diffusion. In the next section we review the classical theory of hyperbolic conservation laws with non-convex fluxes of the form (13). Later in that section we show that for the case of a convex flux, a regularization of the form (12) has similar dynamics to lower order regularizations. However, the interaction of the non-convex flux and fourth order diffusion, which we discuss in Section 4, produces a dramatically different behavior.

3 Lax shocks, rarefactions, and traveling waves

Although the parameter D in equation (12) is typically small in experiments that have been carried out to date, it is instructive to consider the effect of second order diffusion, neglecting the fourth order diffusive term that is of central importance in this paper. Moreover, it is likely that future experiments will explore parameter ranges where D is not negligibly small, and may provide the dominant diffusive effect. For these reasons, in Subsection 3.1, we discuss the case of second order diffusion in the absence of fourth order diffusion, but maintaining the non-convex flux function. In Section 3.2, we focus on fourth order diffusion, but consider only a convex flux function. In both of these subsections, we summarize known results in order to set the context for consideration in Section 4 of fourth order diffusion with a non-convex flux.

3.1 Lax shocks with second order diffusion

In this subsection, we study the following equation with second order diffusion:

$$h_t + [f(h)]_x = \delta (h^3 h_x)_x. \tag{14}$$

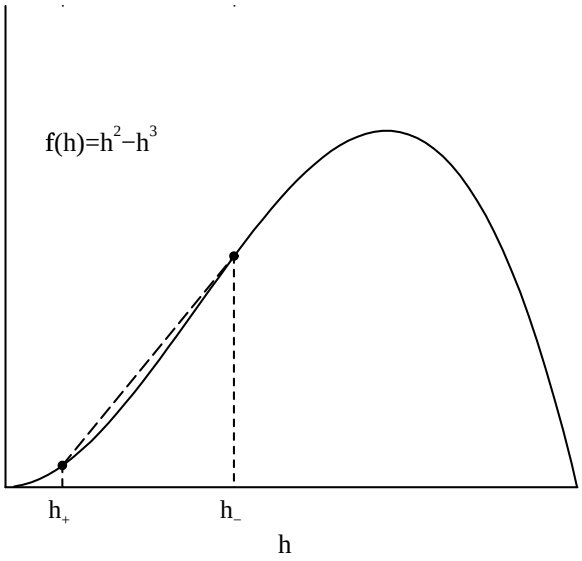

Fig. 2. Flux function f(h) and a shock wave (19) satisfying (22).

where $f(h)$ is the non-convex flux function

$$f(h) = h^2 - h^3$$

depicted in Fig. 2, and $\delta > 0$ is a small parameter. Note that the flux function $f(h)$ has a global maximum at

$$h_{max} = \frac{2}{3}$$

and an inflection point at

$$h_I = \frac{1}{3}.$$

To leading order (i.e., $\delta = 0$ in equation (14)), solutions satisfy the scalar conservation law

$$h_t + f(h)_x = 0. \tag{15}$$

Smooth solutions of (15) can be found implicitly using the method of characteristics:

$$h(x,t) = h_0(x - f'(h(x,t))t), \tag{16}$$

where $f'(h) = 2h - 3h^2$ is the characteristic speed. However, as t increases, solutions of (16) typically undergo bifurcations to multi-valued profiles, corresponding to the formation of shock waves in solutions of (15). To investigate these discontinuous solutions, we consider the Riemann problem, consisting of equation (15), together with initial data of

the form

$$h(x,0) = \begin{cases} h_\infty, & \text{if} \quad x < 0, \\ b, & \text{if} \quad x > 0. \end{cases} \tag{17}$$

This is a classical initial value problem in scalar conservation laws (see e.g. [36]). Since f is non-convex, the classical solution has slightly more structure than for a convex flux function. In this section, we describe the classical solution, justifying it in part through equation (14), which has only second order diffusion. In Section 4, we shall see that the classical solution does not always reflect the leading order behavior when considering *fourth* order diffusion.

Since the Riemann problem is scale invariant, we seek solutions that possess this property, and hence are functions of x/t. For $b < 1/3$ and $h_\infty > b$, the context in which we are interested, there are two types of classical solution, namely a single shock wave, and a rarefaction-shock. To describe these more precisely, we consider in turn rarefaction waves, shock waves and finally rarefaction-shocks.

A *centered rarefaction wave* is a solution of (15) of the form $h(x,t) = h_R(x/t)$, where h_R is continuous and piecewise C^1. Substituting into (15), we find

$$h_R'(\xi)[f'(h_R) - \xi] = 0$$

so that either $h_R' = 0$ (i.e., h_R is constant) or $h_R(\xi) = {f'}^{-1}(\xi)$. More specifically (possibly restricting x/t to an interval)

$$h(x,t) = \begin{cases} h_- & \text{if} \quad x \le f'(h_-)t \\ h_R(x/t) & \text{if} \quad f'(h_-)t \le x \le f'(h_+)t \\ h_+ & \text{if} \quad f'(h_+)t \le x \end{cases} \tag{18}$$

is a rarefaction wave if $f'(h_R(\xi)) = \xi, f'(h_-) \le \xi \le f'(h_+)$, and either $h_- < h_+ < 1/3$, or $1/3 < h_+ < h_-$.

A *centered shock wave*

$$h(x,t) = \begin{cases} h_- & \text{if} \quad x < st \\ h_+ & \text{if} \quad x > st, \end{cases} \tag{19}$$

with speed s is a weak solution of (8) if the triple (h_-, h_+, s) satisfies the Rankine-

Hugoniot condition

$$-s(h_+ - h_-) + f(h_+) - f(h_-) = 0. \tag{20}$$

Thus the shock speed

$$s = \left(f(h_+) - f(h_-)\right)/(h_+ - h_-) \tag{21}$$

is the slope of the chord joining the points $(h_\pm, f(h_\pm))$ in the graph of f, as illustrated in Figure 2.

A shock (19) is called *compressive,* or a *Lax shock* if it satisfies the Lax entropy condition [37], which relates the slope of the chord, given by (21), to the characteristic speeds, which are slopes (derivatives) of f:

$$f'(h_+) < s < f'(h_-). \tag{22}$$

We derive equation (22) in Section 7 using entropies, for a regularization of the type (14) with *linear* second order diffusion (the result is the same with nonlinear diffusion). These bounds are rather different from those that we derive for the fourth order regularization in (10).

It is straightforward to verify that when the flux function f has at most one inflection point, every Lax shock (19) has a traveling wave solution $h(x,t) = h_{Lax}(\frac{x-st}{\delta})$, of the viscous equation (14), satisfying

$$h_{Lax}(\pm\infty) = h_\pm; \quad h'_{Lax}(\pm\infty) = 0.$$

Thus, by neglecting surface tension, all Lax shocks are admissible in the sense that they are $\delta \to 0$ limits of traveling wave solutions of the regularized equation (14). We refer to the traveling wave solution h_{Lax} as a *viscous profile.*

Conversely, the family of shock waves (19) possessing viscous profiles consists of Lax shocks, together with shocks for which one of the inequalities (22) is an equality, so that characteristics are parallel to the shock on one side – the shock speed is characteristic. These shocks are sometimes known as generalized Lax shocks, as they are limits of Lax shocks. Generalized Lax shocks are part of the construction of rarefaction-shock waves. In such a wave, $h(x,t) = h_{RS}(x/t)$, is piecewise C^1, with a generalized Lax shock at the leading edge (largest x/t) of a rarefaction wave. Thus, the shock is characteristic on the

left. Specifically,

$$h_{RS}(\xi) = \begin{cases} h_- & \text{if} \quad \xi \le f'(h_-) \\ h_R(\xi) & \text{if} \quad f'(h_-) \le \xi \le f'(h_m) \\ h_+ & \text{if} \quad f'(h_m) < \xi, \end{cases} \tag{23}$$

where h_R represents a rarefaction wave, and h_m satisfies $f'(h_m) = (f(h_m) - f(h_+))/(h_m - h_+)$, which equates the shock speed with the characteristic speed at h_m; equivalently, the chord from $(h_+, f(h_+))$ to $(h_m, f(h_m))$ in the graph of f is tangent at $h = h_m$. For the specific flux $f(h) = h^2 - h^3$, we have $h_m = (1 - h_+)/2$.

We can now describe solutions of the Riemann problem (15,17), for the parameter ranges $b < 1/3$ and $h_\infty > b$ of interest. Let $h_b = (1 - b)/2$.

(1) If $b < h_\infty < h_b$ then the solution is a single Lax shock

$$h(x,t) = \begin{cases} h_\infty, & x < st, \\ b, & x > st, \end{cases}$$

where the shock speed s is given by (21):

$$s = h_\infty + b - h_\infty^2 - h_\infty b - b^2. \tag{24}$$

(2) If $h_\infty > h_b$, then the solution is a rarefaction–shock (23) in which $h_- = h_\infty, h_m = h_b, h_+ = b$.

The rarefaction-shock solution (23) was introduced by Ludviksson and Lightfoot [39] as a first order approximation (neglecting curvature) of the advancing front observed in their thermally driven coating flow experiments. In Section 4 we show that including the curvature effects by introducing the fourth order diffusion in (10) from surface tension yields dramatically different behavior for thicker films. Instead of the rarefaction-shock in (23) we obtain a rarefaction-undercompressive shock, in which the undercompressive shock separates from the rarefaction wave. It is interesting to note that Ludviksson and Lightfoot found experimental front speeds up to 40% slower (but never faster) than predicted by (23). This could be explained by the presence of an undercompressive shock, which travels at a slower speed than the shock in (23), as discussed in more detail in [4] for the case of intermediate film thicknesses.

3.2 Burgers flux with fourth order nonlinear diffusion

Before addressing the problem with both surface tension and gravity (i.e. a non-convex flux function and a fourth order nonlinear diffusion) we review the problem with surface tension and surface tension gradients but neglecting gravity. Here the equation is

$$h_t + (\frac{\tau h^2}{2\eta})_x = -\frac{\gamma}{3\eta}(h^3 h_{xxx})_x.$$

As in [33], we can rescale the equation to have the form (this is a different rescaling than that of Section 2)

$$h_t + (h^2)_x = -(h^3 h_{xxx})_x. \tag{25}$$

Without the competing effect of gravity, the flux function is convex. Equation (25) is a nonlinear fourth order regularization of Burgers equation.

Consider the traveling wave problem for (25) with

$$h \to 1 \quad \text{as} \quad x \to -\infty \quad \text{and} \quad h \to \tilde{b} \quad \text{as} \quad x \to \infty. \tag{26}$$

In Theorem 1, we prove that whenever $\tilde{b} < 1$, there is a traveling wave solution $h(x - st)$ moving with speed $s = 1 + \tilde{b}$. These capillary profile solutions are fourth order (nonlinear [1]) regularizations of the classical Lax shock for the inviscid Burgers equation. They have been computed numerically in [33] for several values of $\tilde{b}$ between 0.01 and 0.9.

Asymptotic analysis suggests that as in the case of gravitationally driven thin films [3,46] (for which $f(h) = h^3$) the structure of the capillary ridge or"bump", in traveling wave solutions of (25), has a singular limit in which the height of the bump becomes unbounded as $\tilde{b} \to 0$. It is interesting to note that the non-convex flux function in (10), in which gravity is included, yields solutions with a fundamentally different singular limit as $b \to 0$. For very small b, the dominant behavior at the leading edge of the front is always an undercompressive shock (see the following sections) which has a height that is always bounded by 1. To summarize, we expect that as $b \to 0$, for (10) the front speed goes to zero while the undercompressive shock height goes to 1, while in the case of the convex fluxes ($f(h) = h^2$ or h^3) the front speed approaches a constant (1 in the case of (26)) while the bump height becomes unbounded.

Following a general topological argument of Michelson [41] (see also Renardy [42] for an application to surfactant driven thin films) we now prove the existence of capillary shock profiles for Lax shocks. We use some ideas of the proof in Section 7 to prove rigorous bounds on capillary profile solutions to equation (10).

[1] Capillary profiles for fourth order *linear* regularizations of Burgers equation have been studied in [40,41,15,35]

Theorem 1 *Given any $\tilde{b} > 0$ such that $\tilde{b} < 1$, there exists a bounded positive traveling wave solution $h(x - st)$ of (25) with far field limits* (26).

PROOF: Going into a traveling reference frame, we note that if the problem with surface tension has a capillary shock, it will be a traveling wave solution that reduces to solving a third order equation

$$h_{xxx} - \frac{s}{h^2} + \frac{1}{h} - Q\frac{1}{h^3} = 0 \tag{27}$$

where the speed $s = 1 + \tilde{b}$ and $Q = -\tilde{b}$. We look for a solution of (27) that goes to 1 as $x \to -\infty$ and to $\tilde{b}$ as $x \to \infty$.

The proof of existence has three parts: (1) Establish the existence of a Lyapunov function, (2) show that the Lyapunov function can be used to show compactness of the set of bounded solutions and (3) deform the equation continuously in order to apply a topological (Conley index) argument to prove existence.

To carry out the first part, multiplying by h_x, the ODE (27) may be written in terms of the Lyapunov function

$$L(h) = h_{xx}h_x + R(h)$$

where

$$R'(h) = -\frac{s}{h^2} + \frac{1}{h} - Q\frac{1}{h^3}.$$

Thus

$$(L(h))_x = (h_{xx})^2$$

so that the Lyapunov function is increasing.

Now we show that the set of all bounded solutions of (27) is compact in $C^3(\mathbb{R})$. To do this, we first derive a priori upper and lower bounds for bounded solutions of (27). Then we show that this leads to a priori bounds for higher derivatives. This then leads to compactness in C^3.

First note that any bounded solution of (27) connects two zeros of $R'(h)$, and the only choices are $\tilde{b}$ and 1. Since $L(h) \to R(h)$ as $x \to \pm\infty$ for any bounded solution h, and $R(\tilde{b}) > R(1)$ we see that the only possible bounded solutions are the fixed points $\tilde{b}$ and 1 and possibly a heteroclinic orbit connecting these two states. Since $h_x h_{xx}$ vanishes at an extremum of a solution, all bounded solutions h must have $R(1) < R(h) < R(\tilde{b})$. From the structure of R, we see that there is a value h_* below $\tilde{b}$ and a value h_{**} above 1 such that $R(h_*) = R(\tilde{b})$ and $R(h_{**}) = R(1)$. All bounded solutions must lie between h_* and h_{**}:

$$h_* < h < h_{**}.$$

See Fig. 3 for a diagram.

These a priori upper and lower bounds imply via (27) that h_{xxx} is uniformly bounded in L^∞. To derive a priori bounds on intermediate derivatives, we note that the Lyapunov

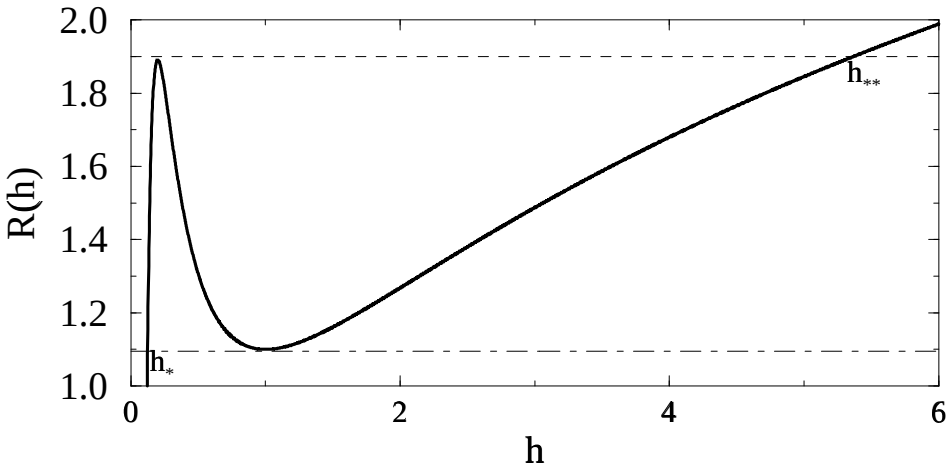

Fig. 3. The function R in the Lyapunov function. Shown the case $\tilde{b} = 0.2$. Any orbit connecting 1 to $\tilde{b}$ must have all of its extrema lie between h_* and h_{**}.

function implies that any bounded solution satisfies

$$\int_{-\infty}^{\infty} (h_{xx})^2 dx = R(h_+) - R(h_-) < C,$$

where $h_\pm = h(\pm\infty)$, which implies, by the Sobolev lemma and the fact that h_x has mean zero, an a priori bound on the L^∞ norm of h_x. The second derivative can be bounded in L^∞ by a standard interpolation argument. Also, differentiating equation (27) and applying the known bounds for lower derivatives gives a priori bounds for all higher derivatives.

To show that the set of all bounded solutions is compact in $C^3(\mathbb{R})$, we consider a sequence h_i of bounded solutions. Given any compact interval $[-K, K]$, the functions $(h_i)_{xxx}$ form an equicontinuous family. Thus, there is a subsequence that converges in $C^3[-K, K]$ to a function h which necessarily satisfies (27). A diagonalization argument in i and K completes the proof of compactness in $C^3(\mathbb{R})$.

In order to apply Conley index theory, we deform (27) to an ODE with no critical points. Consider a smooth family of ODEs

$$h_{xxx} + \beta - \frac{s}{h^2} + \frac{1}{h} - Q\frac{1}{h^3} = 0 \tag{28}$$

parameterized by β. Denote by L_β the modified Lyapunov function $L_\beta = h_x h_{xx} + R(h) + \beta h$. Let $h_I \in [\tilde{b}, 1]$ denote the position of the inflection point of R. Denote $\beta_0 = -R'(h_I)$. For $0 < \beta < \beta_0$, the modified ODE (28) also has the same structure as (27) and we see that solutions of the modified equation can be bounded between $h_{*,\beta} > h_*$ and $h_{**,\beta} < h_{**}$. Moreover, we can bound the higher derivatives of h as before.

We now apply a topological argument to finish the proof. For $\beta > \beta_0$, the set of bounded solutions is empty. The Conley index is a homotopy invariant associated with isolated sets of bounded solutions. For $\beta > \beta_0$, the Conley index for the empty set is different from that of a set of hyperbolic fixed points. Therefore, for $\beta = 0$ there must be a non-trivial bounded solution and, as we have shown above, the only choice is one connecting 1 to $\tilde{b}$. $\square$

4 Dynamics of the PDE and undercompressive capillary shocks

In this section and the next, we consider (10) with $D = 0$, namely

$$\boxed{h_t + (h^2 - h^3)_x = -(h^3 h_{xxx})_x.} \tag{29}$$

Equation (29) corresponds physically to a vertical incline or also the case where τ^2 is small compared with $\gamma\rho g$. In this section, we present some case studies of numerical simulations of the PDE (29), showing that a range of strong Lax shocks are no longer admissible and that a double shock structure forms involving an undercompressive wave. This kind of phenomenon was observed recently [23] for diffusive-dispersive equations of the form

$$h_t + (\tilde{f}(h))_x = \alpha h_{xx} + \beta h_{xxx}$$

in which $\tilde{f}$ is non-convex. In the next section, we explain the transition from weak capillary shock profiles to the undercompressive structure via a study of the ODE describing traveling wave solutions of (29).

The numerical scheme used to solve (29) is the same scheme used to generate the traveling wave profiles in [3], a finite difference scheme with a fully implicit time step and spatial derivatives based on centered differences. The discretization of the fourth order term is described in detail in [8]. The centered difference approximation of the convective term coupled with the implicit time step produces a modified equation [19] that to first order in Δt and Δx introduces second order numerical diffusion into (29):

$$h_t + (f(h))_x = \frac{\Delta t}{2}(f'(h)^2 h_x)_x - (h^3 h_{xxx})_x.$$

The implicit time step produces a stable scheme with large Δt, however the numerical diffusion causes this stable method to give the wrong value for the undercompressive shock height when Δt is too large. This indicates that the structure of the undercompressive shocks may change significantly when second order diffusion is present (as in the case of moderately large D in equation (10)). The numerical diffusion can be globally reduced by taking a sufficiently small Δt and locally reduced by using a reference frame moving with the speed of the front. Each strategy was used when needed.

In the numerical solutions of initial value problems, we observe various patterns of propagating waves. In describing these waves, we use the terms shock wave and traveling wave interchangeably, identifying pieces of the solution that appear to be traveling waves with the shock wave solutions of the underlying conservation law. Similarly, we speak of compressive and undercompressive waves when the underlying shock waves have the corresponding property. All of the computations are performed in a traveling reference frame moving with speed

$$s(h_\infty, b) = \frac{f(h_\infty) - f(b)}{h_\infty - b} = h_\infty + b - (h_\infty^2 + h_\infty b + b^2).$$

In some cases, we find a traveling wave solution with that speed and in other cases we do not. All cases discussed below consider $b = 0.1$ however the same qualitative dynamics emerge for all $0 < b < 1/3$.

Case 1: $b < h_\infty < h_1$. Weak Lax shock profiles.

For somewhat small values of h_∞, near b, the solution of the PDE settles down to a unique capillary shock profile connecting the states h_∞ and b. For example, consider initial data of a smoothed shock profile

$$h(x) = (\tanh(-x + 100) + 1)\frac{h_\infty - b}{2} + b$$

connecting the states h_∞ as $x \to -\infty$ to b as $x \to \infty$. Fig. 4 shows a plot of the solution for $h_\infty = 0.3$ and $b = 0.1$. The solution at later times, computed in a reference frame moving wiht speed $s(0.3, 0.1)$, settles down to the unique traveling wave solution for these boundary conditions. This behavior persists up to a value of h_∞ which we call h_1; it depends on b.

Case 2: $h_1 < h_\infty < h_2$. Multiple Lax shock profiles.

For h_∞ in a range, $h_1 < h_\infty < h_2$, where h_2 also depends on b, there are multiple capillary shock profiles connecting the same two left and right states, respectively h_∞ and b. Some of these profiles are stable for the PDE (29) and others are not. In Fig. 5, we show several solutions with $b = 0.1$ and $h_\infty = 0.3323$.

For the solution shown in Fig. 5a, we used the initial condition

$$h_0(x) = (\tanh(-x + 300) + 1)\frac{h_\infty - b}{2} + b. \tag{30}$$

One might expect all profiles with the same far field boundary conditions as (30) to settle down to this profile. However, if we start with the initial condition

$$h_0(x) = \begin{cases} \frac{(0.6-h_\infty)}{2}\tanh((x - 300)) + \frac{(0.6+h_\infty)}{2}, & x < 305, \\ -\frac{(0.6-b)}{2}\tanh((x - 310)) + \frac{(0.6+b)}{2}, & x > 305, \end{cases} \tag{31}$$

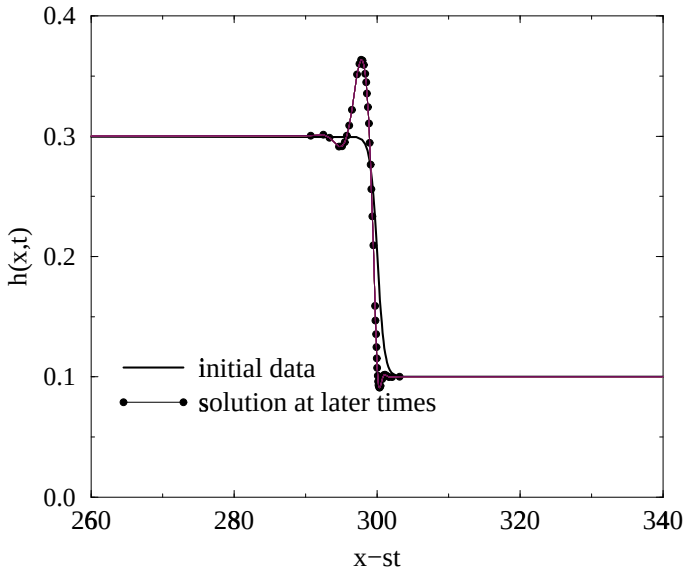

Fig. 4. The Lax shock with surface tension. Here b=0.1, $h_\infty = 0.3$.

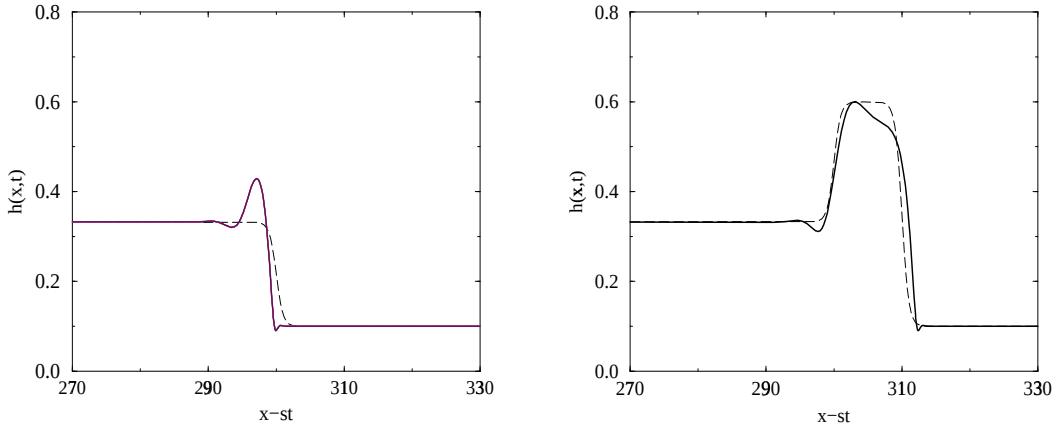

(a) (b)

Fig. 5. Two stable traveling waves with the same values $b = 0.1, h_\infty = 0.3323$. The computations are done in a traveling reference frame moving with shock speed $s(h_\infty, b)$. Solid lines are the solutions at very late times.

which introduces a bump, we observe (see Fig. 5b) that the solution approaches a different traveling wave profile moving with the same speed and connecting the same left and right states.

In the next section, we study more carefully the ODE for the traveling wave profiles and show via numerical computations in phase space that there are actually *four* traveling

waves for this pair of values $h_\infty = 0.3323$ and $b = 0.1$. Two (the ones depicted in Fig. 5) are stable with respect to the PDE evolution and the other two are not.

In addition to the two stable profiles shown in Fig. 5, there is another possibility for the dynamics. In Fig. 6, we take the initial condition to be

$$h_0(x) = \begin{cases} \frac{0.6-h_\infty}{2}\tanh((x-300)) + \frac{(0.6+h_\infty)}{2}, & x < 310 \\ -\frac{(0.6-b)}{2}\tanh((x-320)) + \frac{(0.6+b)}{2}, & x > 310, \end{cases} \tag{32}$$

with a broader hump than in (31), but of the same height. The solution does not settle down to a single traveling wave. Instead, two shocks emerge, an *undercompressive wave* on the right connecting b to a larger state $h_{UC} \approx 0.568$, followed by a slower compressive wave connecting h_{UC} to h_∞. Both waves travel more slowly than the traveling waves of Fig. 5.

For each $b < 1/3$, there is special value, h_{UC}, for h_∞ for which an undercompressive traveling wave exists. That is, there is a capillary shock profile connecting h_{UC} to b. The corresponding shock wave is undercompressive in the sense that it is supersonic on both sides, i.e., the characteristic speed is smaller than the wave speed on both sides of the shock. Correspondingly, the chord connecting h_{UC} to b in the graph of the flux cuts through the flux curve at an intermediate point $h_* = 1 - h_{UC} - b$. In Fig. 7, we show the "undercompressive connections" for various values of b. These were obtained by reading off the constant value of h that emerges between the undercompressive traveling wave and the compressive traveling wave, as in Fig. 6. We also confirmed these results via the ODE computations in the next section.

Case 3: $h_2 < h_\infty < h_{UC}$. Undercompressive double shock structures.

For h_∞ in this range, *there are no capillary shock profiles joining h_∞ to b*. In contrast to Case 2, for $h_2 < h_\infty < h_{UC}$, all initial conditions that we tested converge to a solution with the same double shock structure. Fig. 8 illustrates this behavior for the case $h_\infty = 0.4$ and $b = 0.1$. The initial condition is a smoothed step function from $h_\infty = 0.4$ to $b = 0.1$. It is shown by the dashed line in the plot. The solution at a later time has two shocks. The leading shock is the undercompressive shock and the trailing shock is a classical Lax shock.

Case 4: $h_\infty > h_{UC}$. Rarefaction-undercompressive shock.

For this case, we see a combination rarefaction wave and undercompressive shock. Recall from Section 2 that in the case where surface tension is absent, when $h_\infty > (1-b)/2$, an initial step profile evolves as a rarefaction-shock combination, given by the solution in (23). However, for the problem with fourth order diffusion, a capillary shock profile connecting $(1-b)/2$ to b typically does not exist and instead the rarefaction connects to the undercompressive shock connecting h_{UC} to b. Since the undercompressive shock moves with a speed $s(h_{UC}, b)$, which is greater than the speed $f'(h_{UC})$, of the right hand side (leading edge) of the rarefaction wave, the undercompressive shock separates from

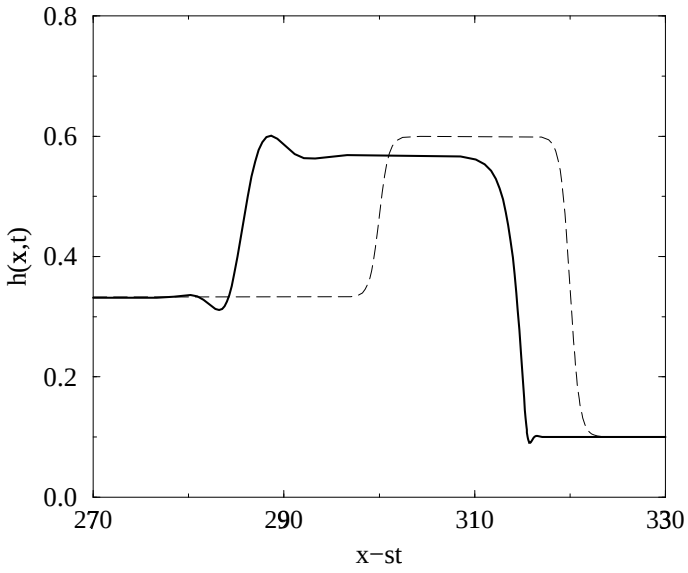

Fig. 6. Solution with an undercompressive wave (on the right) and a compressive wave. The dashed line is the initial condition (32); the dark line is the solution at time 10^5. Note that the traveling reference frame is the same as in Fig. 5.

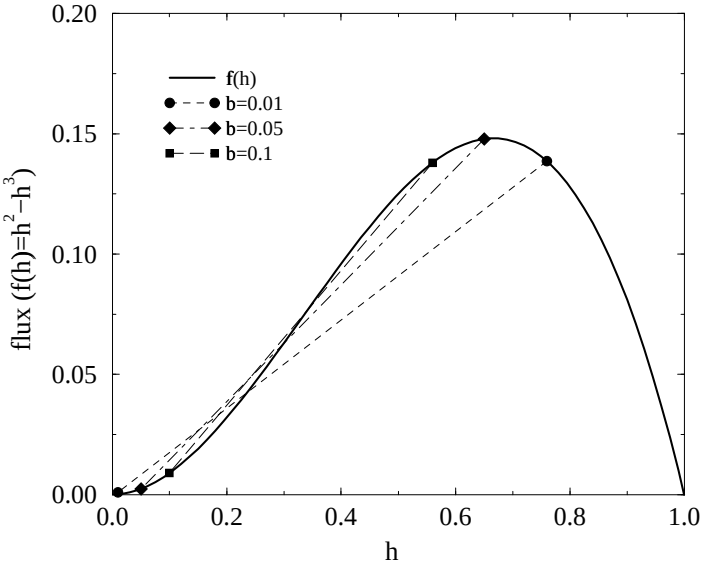

Fig. 7. The undercompressive connection. Here we compare $b = 0.1, 0.05, 0.001$. Shown is the connection from b to the state h_{UC}.

the rarefaction wave to produce a separated rarefaction-shock profile. At large times or, via rescaling the equation, when ϵ is small in (12), we expect that the solution of the PDE with approximate Riemann initial data will approximate the non-classical inviscid

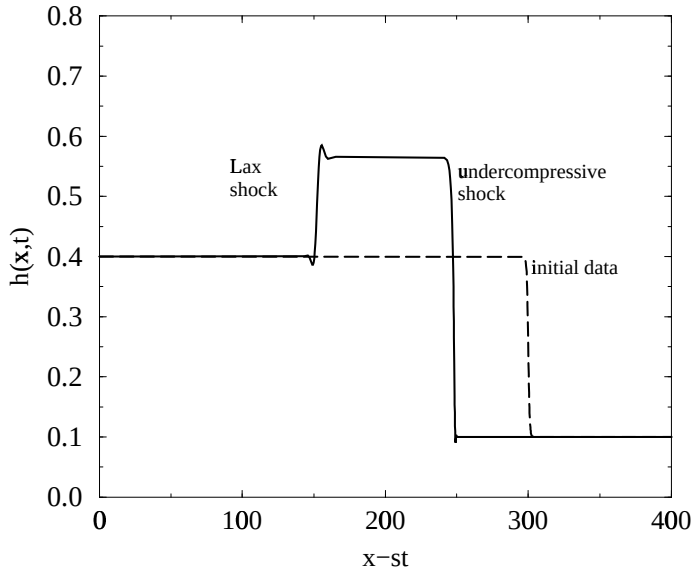

Fig. 8. Undercompressive double shock structure for $h_\infty = 0.4$ to $b = 0.1$ at time 4800.

rarefaction-undercompressive shock solution given by

$$h_{RUS}(\xi) = \begin{cases} h_\infty & \text{if} \quad \xi \le f'(h_\infty) \\ h_R(\xi) & \text{if} \quad f'(h_\infty) \le \xi \le f'(h_{UC}) \\ h_{UC} & \text{if} \quad f'(h_{UC}) \le \xi \le s(h_{UC}, b) \\ b & \text{if} \quad s(h_{UC}, b) < \xi, \end{cases} \tag{33}$$

where $\xi = x/t$ is the similarity variable and as in Section 2, $h = h_R$ denotes the rarefaction wave.

The following numerical example confirms this prediction. Here we consider $b = 0.1$ and $h_\infty = 0.8$, with initial condition

$$h(x) = (\tanh(-x + 1100) + 1)\frac{h_\infty - b}{2} + b. \tag{34}$$

The initial data are centered at $x = 1100$ simply so that the rarefaction remains in the regime of positive $x - st$ for the duration of the simulation. Here, $s = s(0.8, 0.1) = 0.17$, is the speed of the reference frame and the time step is chosen small enough to minimize dissipative errors from numerical diffusion. The computed solution of (29) starting with this initial condition does indeed evolve into a rarefaction-shock combination, in which

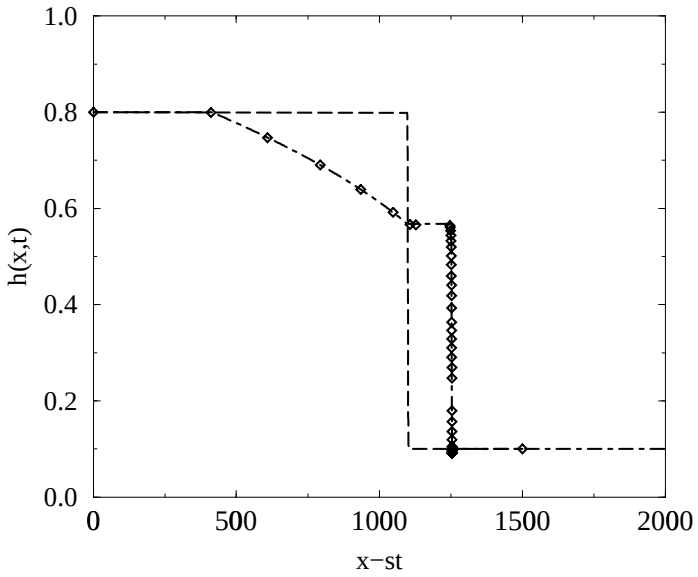

Fig. 9. A rarefaction undercompressive shock solution for smoothed Riemann initial data with $h_\infty = 0.8$ and $b = 0.1$. The initial condition (34) is shown as a dashed line and the numerical solution at time $t = 1400$ is shown as diamonds. The theoretical inviscid non-classical rarefaction-shock is shown as a dot-dashed line.

the shock is the undercompressive shock from h_{UC} to $b = 0.1$, which separates from the rarefaction wave. Shown in Fig. 9 are the initial condition (dashed line), the PDE solution at time $t = 1400$ (a subset of the computational values are shown as diamonds) and the expected inviscid limit of the rarefaction-undercompressive shock combination in (33) at $t = 1400$ (shown as a dot-dashed line). Note that the latter two are almost identical, except where the fourth order diffusion smooths the shock and the connection to the rarefaction.

5 Traveling waves with fourth order diffusion.

In this section, we examine traveling wave solutions of equation (29). These solutions satisfy the third order ordinary differential equation

$$-s(h - h_-) + f(h) - f(h_-) = -h^3 h''', \tag{35}$$

where $h_- = \lim_{\xi \longrightarrow -\infty} h(\xi)$. (In integrating the equation once, we have assumed $h'''(\xi) \longrightarrow 0$ as $\xi \longrightarrow -\infty$.)

Equation (35) has two parameters h_- and s. For the present, the singularity at $h = 0$ is unimportant; we take $h_- > 0$ and restrict h to be bounded away from zero.

Writing (35) as

$$h''' = g(h; h_-, s) \tag{36}$$

where

$$g(h; h_-, s) = -h^{-3}\left(-s(h - h_-) + f(h) - f(h_-)\right), \tag{37}$$

we see that equilibria $h = h_+$ (zeroes of $g(.; h_-, s)$) are given by the Rankine-Hugoniot condition (20) for shocks. Moreover, the linearized ordinary differential equation $u''' = \frac{\partial g}{\partial h}(h_+; h_-, s)u$ has three eigenvalues, namely the three cube roots of $\frac{\partial g}{\partial h}(h_+; h_-, s)$. Note further that $\frac{\partial g}{\partial h}(h_+; h_-, s) = -\frac{1}{h_+^3}(f'(h_+) - s)$, so that the sign of $\frac{\partial g}{\partial h}(h_+; h_-, s)$ is related to whether characteristics at h_+, traveling with speed $f'(h_+)$, are faster or slower t han the speed s of the traveling wave.

To further understand equilibria, and trajectories joining different equilibria, we write equation (36) as a first order system:

$$\begin{aligned} h' &= v \\ v' &= w \\ w' &= g(h; h_-, s). \end{aligned} \tag{38}$$

For a specific equilibrium $(h, v, w) = (h_+, 0, 0)$, with $g(h_+; h_-, s) = 0$, the three cube roots of $\frac{\partial g}{\partial h}(h_+; h_-, s)$ give rise to the following structure of invariant manifolds containing the equilibrium.

(i) If $f'(h_+) < s$, then $\frac{\partial g}{\partial h}(h_+; h_-, s) > 0$, so that $(h_+, 0, 0)$ has a one-dimensional unstable manifold and a two dimensional stable manifold on which solutions spiral into the equilibrium due to the complex conjugate pair of eigenvalues with negative real part.

(ii) If $f'(h_+) > s$, then $\frac{\partial g}{\partial h}(h_+; h_-, s) < 0$, so that $(h_+, 0, 0)$ has a one-dimensional stable manifold and a two dimensional unstable manifold on which solutions spiral away from the equilibrium due to the complex conjugate pair of eigenvalues with positive real part.

Now equilibria of (38) correspond to intersections of the line with slope s through $(h_-, f(h_-))$ with the graph of f. Alternatively, we can fix $h_+ \neq h_-$ and define s through the Rankine-Hugoniot condition (20). Specifically, for the flux function $f(h) = h^2 - h^3$,

$$s = h_- + h_+ - h_-^2 - h_-h_+ - h_+^2. \tag{39}$$

Consider the case of a weak Lax shock, specifically $0 < h_+ < h_- < 1/3$, with $h_- - h_+$ small. Then $(h_-, 0, 0)$ has a two-dimensional unstable manifold and $(h_+, 0, 0)$ has a two-dimensional stable manifold. If they intersect transversally (away from the equilibria), then the curve of intersection is a trajectory for (38) from $(h_-, 0, 0)$ to $(h_+, 0, 0)$. We refer

to the corresponding solution of the partial differential equation (29) as a capillary shock profile from h_- to h_+.

The existence of capillary shock profiles for weak Lax shocks away from the inflection point $h = 1/3$ is provided by the analysis of Kopell and Howard [35].

Theorem 2 *Let $0 < h_+ < 1/3$. There exists $\epsilon = \epsilon(h_+) > 0$ such that if $0 < h_+ < h_- < h_+ + \epsilon$, then there is a capillary shock profile from h_- to h_+.*

Note that while Theorem 1 concerns the existence of arbitrarily strong capillary shock profiles for Lax shocks, the proof depends on the convexity of the flux function. In Theorem 2, the flux is non-convex, but the hypotheses are designed to relegate the non-convexity to higher order terms which do not affect the existence of the traveling wave profiles. It might be possible therefore to modify the proof of Theorem 1 so that it applies to Theorem 2, but instead we appeal directly to the result of Kopell and Howard.

In the following subsection we discuss numerical computations of the structure of phase space in order to identify values of h_- for which there are capillary shock profiles for Lax shocks, and to understand transitions in the vector field (38). In a recent paper [34], Kataoka and Troian compute several trajectories for the ODE (36), and discussed the stability of the corresponding traveling waves to two-dimensional perturbations. In the subsequent subsection we discuss the stability of the capillary shock profiles with respect to the dynamics of the PDE (29). In Section 7 we derive a priori upper and lower bounds for capillary shock profiles, and also derive an upper bound on the values of h_- for which capillary shock profiles exist.

5.1 Structure of phase space

We next investigate the appearance of capillary shock profiles for different h_- by numerically exploring the structure of the phase space. In order to do so, we determine the unstable and stable manifolds of the three equilibria

$$B = (h_+, 0, 0), \quad M = (h_-, 0, 0), \quad \text{and} \quad T = (1 - h_- - h_+, 0, 0),$$

(with $h_+ < h_- < 1 - h_- - h_+$) by integrating (36) either forwards or backwards in ξ, respectively, starting with initial data $(h(0), h'(0), h''(0))$ at a distance of about 10^{-7} from an equilibrium. The necessary computations were carried out using the explicit Adams method of the LSODE package [25], which features automatic step size selection and adaptivity.

Certain trajectories are visualized in a perspective plot of the three-dimensional phase space. Additionally, we show the intersection of the stable manifold $W^s(B)$ of B, the unstable manifold $W^u(M)$ of M, and the unstable manifold $W^u(T)$ of T with the plane

$$P = \{(h, h', h'');\ h = (2h_- + h_+)/3\}.$$

We refer to the plane P as a Poincaré section. Since $W^s(B)$ and $W^u(M)$ are surfaces, their intersections with P appear as two curves, whereas the one-dimensional manifold $W^u(T)$ appears in the Poincaré section as a point. Capillary profiles for Lax shocks correspond to intersections of $W^u(M)$ and $W^s(B)$. A capillary profile for an undercompressive shock appears when $W^s(B)$ contains the curve $W^u(T)$.

In the discussion below, we assume $h_+ = b = 0.1$; however, the same qualitative picture emerges for other positive values of $b < 1/3$. We discuss the dynamics of the phase space for b close to $1/3$ in the next section. The results of the computations are shown in Figs. 10-15, for values of h_- increasing from 0.3 to 0.355. The notation for the different curves and significant points carries over from one figure to the next, with new symbols added as needed. We discuss in turn three cases, corresponding to the first three cases identified in Section 4. (Case 4 of Section 4 is the same as Case 3 here, because of the parameterization of the vector field by h_-, which is always taken to be the middle equilibrium in this section.)

Case 1: $h_- < h_1$. Unique capillary shock profile.

For each value of $h_+ < 1/3$ we find a maximum value h_1 for h_-, with the property that there is a unique orbit from M to B provided $h_+ < h_- < h_1$. This is the same h_1 as in the previous section. For $h_+ = 0.1$, we find

$$h_1 = 0.3286.$$

Fig. 10 shows an example with $h_- = 0.3$. The three dimensional phase portrait is shown in Fig. 10(a) with the unstable manifolds $W^u(T)$ and $W^u(B)$ shown as dotted lines. The orbit connecting B to M is shown as a solid line and the orbit from M to T is a dot-dashed line. In Fig. 10(b), the Poincaré section shows that the curves $W^u(M) \cap P$ and $W^s(B) \cap P$ intersect only once, deminstrating uniqueness of the orbit connecting M to B. This orbit corresponds to the traveling wave solution shown in Fig. 4 of Section 4. Note the spiralling structure of $W^u(M) \cap P$. It indicates that the surface $W^u(M)$ winds tightly around the one-dimensional unstable manifold $W^u(T)$ of T, which forms part of its boundary.

Case 2: $h_1 < h_- < h_2$. Multiple capillary shock profiles.

For each value of $h_+ < 1/3$ there is a range of values for $h_- > h_1$, for which there exists more than one orbit connecting M to B. This range of h_- extends up to a finite upper bound h_2, as in the previous section. For $h_+ = 0.1$, we find

$$h_2 = 0.3479.$$

The number of connections can be computed numerically by examining the number of intersection points of the curves $W^u(M) \cap P$ and $W^s(B) \cap P$ on the Poincaré section. We present several computations below, all with $h_+ = 0.1$.

For $h_- = 0.33$, the Poincaré section, shown in Fig. 11(b), indicates three intersections

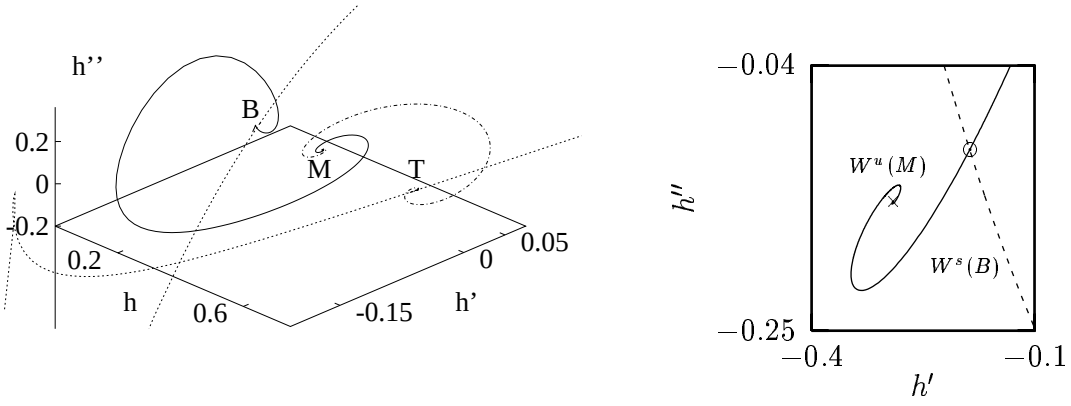

(a) Perspective view

(b) Poincaré section P

Fig. 10. Phase portrait for $h_- = 0.3$: The unique connection from M to T is denoted by a solid line in (a) and appears as the unique intersection point $W^u(M) \cap W^s(B) \cap P$ in (b), $P = \{h = (h_+ + 2h_-)/2\}$. The circle indicates that this connection corresponds to a unique and *stable* traveling wave solution of the PDE (29). The dashed lines on the left are the unstable manifolds of T and B, and a cross in the Poincaré section shows $W^u(T) \cap P$.

of $W^s(B) \cap P$ and $W^u(M) \cap P$. Fig. 11(a) shows the corresponding orbits in three dimensional phase space; on the scale of the graph, two of the orbits nearly coincide with the largest separation near T. Note that $W^u(T)$ comes closer to B than in Case 1 (for which $h_- = 0.3$). However, in both cases $W^u(T)$ follows the same branch of the unstable manifold $W^u(B)$ as $\xi \to \infty$.

As h_- increases from h_1, $W^u(T)$ comes even closer to B until at a special value

$$h_- = h_* = 0.33205,$$

$W^u(T)$ actually connects to B. This special orbit is shown in Fig. 12(a) emphasized with diamonds. The Poincaré section in Fig. 12(b) shows that $W^s(B)$ passes through the center of the spiral structure of $W^u(M)$.

The qualitative structure of the phase space suggests that there are infinitely many turns in $W^u(M) \cap P$, and consequently a countably infinite number of intersections of $W^u(M) \cap P$ with $W^s(B) \cap P$ when $h = h_*$. To understand this, we first remark that, in the neighborhood of T, the connection from M to T is governed by the two complex eigenvalues of the linearization of (38) around this equilibrium. These eigenvalues have negative real part, so that the trajectory approaches T through a spiral with an infinite number of turns. A neighboring trajectory, contained in $W^u(M)$ but not in $W^s(T)$, will initially stay close to the orbit connecting M to T, and undergo some turns, until it finally is repulsed from the vicinity of T along one of the two branches of $W^u(T)$. Since it seems reasonable to expect that an arbitrary number of turns can be achieved just by picking an orbit close enough to the connection from M to T, the spiral structure of

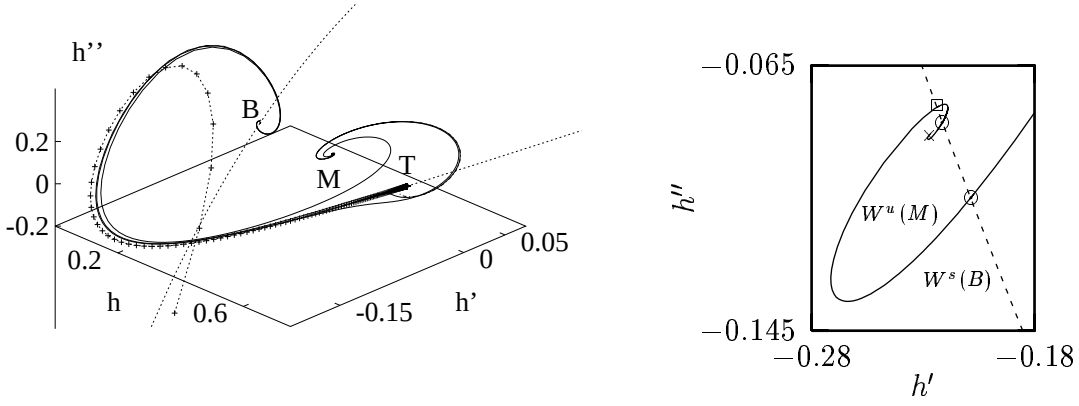

(a) Perspective view

(b) Poincaré section P

Fig. 11. Phase portrait for $h_- = 0.33$: Solid lines on the left represent the three connections from M to T, which appear as three intersection points $W^u(M) \cap W^s(B) \cap P$ in (b). Circles and boxes indicate whether they correspond to stable or unstable traveling wave solutions of the PDE (29), respectively. For better visibility, one branch of $W^u(T)$ has been emphasized with '+'.

$W^u(M)$, which consists of the union of all these individual orbits, can be expected to have an infinite number of turns.

The infinite number of intersections of $W^u(M) \cap P$ with $W^s(B) \cap P$ when $h = h_*$ corresponds to an infinite number of different orbits connecting M to B. Each orbit corresponds to a different traveling wave solution of the PDE (29). All of these traveling waves have the same speed. Note that Fig. 12(b) resolves only a few turns of the spirals of $W^u(M) \cap P$. A closeup of the area at $W^u(T) \cap P$ in Fig. 13 shows at least two more turns of the spiral, and in numerical trials we could resolve a total of six turns and five intersection points, in $W^u(M) \cap W^s(B) \cap P$. The accumulation point of the intersection points in the Poincaré section corresponds to the special orbit connecting T to B. This orbit yields a special traveling wave solution of the PDE (29). This is the undercompressive capillary shock discussed in Case 3 of the previous section. Note that h_* and h_{UC} are related by $h_{UC} = 1 - h_+ - h_*$.

The case $h_* < h_- < h_2$ is analogous to $h_1 < h_- < h_*$. For example, there are two capillary shock profiles in the case $h_- = 0.333$. Note that $W^u(T) \cap P$ now lies on the other side of $W^s(B) \cap P$, see Fig. 14(b). In the three-dimensional plot Fig. 14(a), the unstable manifold of T again gets close to B, but then follows the other branch of $W^u(B)$ as $\xi \to \infty$.

Case 3: $h_2 < h_-$. No capillary shock profiles.

For h_- larger than h_2, $W^s(B) \cap W^u(M) = \emptyset$, implying that there are no orbits from M

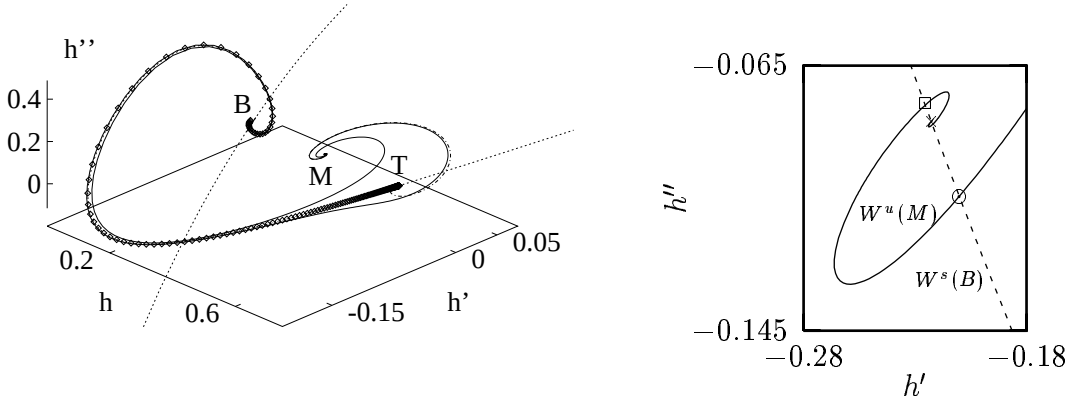

(a) Perspective view

(b) Poincaré section P

Fig. 12. Phase portrait for $h_- = h_* = 0.33205$: Solid lines indicate two of the (probably infinite amount of) connections from M to B in (a), which appear as intersection points in (b). The diamonds in (a) emphasize the special connection from T to B, which only exists for this value of h_-. It corresponds to the undercompressive shock profile of (29). Note that the cross in (b) representing $W^u(T) \cap P$ now is on top of the dotted line for $W^s(B) \cap P$.

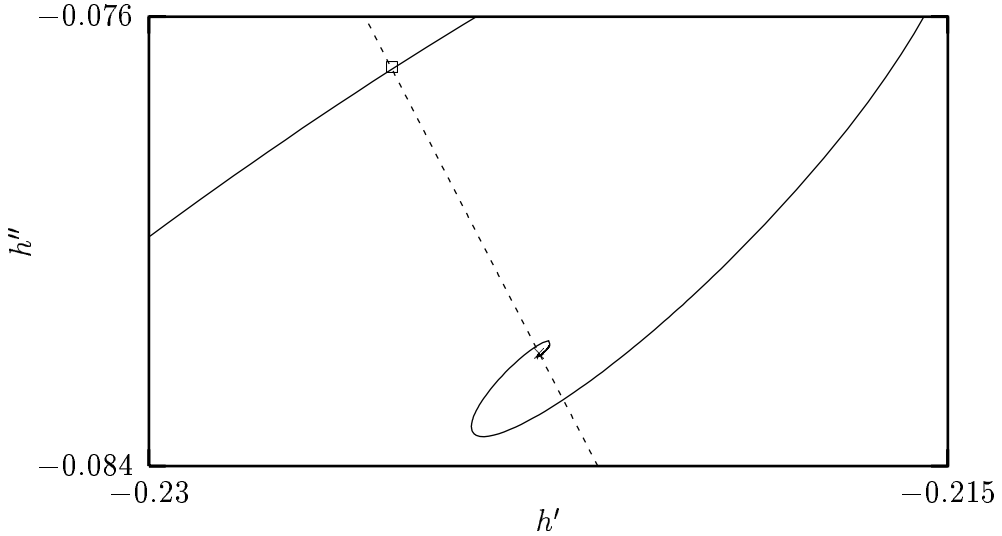

Fig. 13. Close-up of the Poincaré section for $h_- = h_* = 0.33205$, showing additional turns of $W^u(M)$.

to B. Figs. 15(a) and 15(b) show the case $h_- = 0.355$. $W^u(T)$ and $W^u(M)$ have moved further away from $W^s(B)$. The Poincaré section, shown in 15(b), illustrates very well the non-intersection.

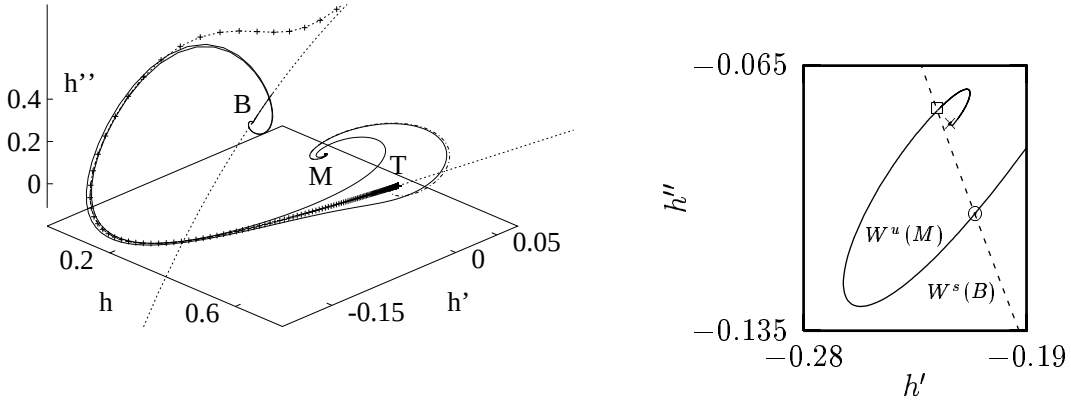

(a) Perspective view (b) Poincaré section P

Fig. 14. Phase portrait for $h_- = 0.333$: Note that $W^u(T)$ gets close to B, then leaves the vicinity of this fixed point along the other branch of $W^u(B) \cap P$ than in Fig. 11(a). Correspondingly, $W^u(T)$ and $W^s(B) \cap P$ have changed sides in the Poincaré section, compared to Fig. 11(b).

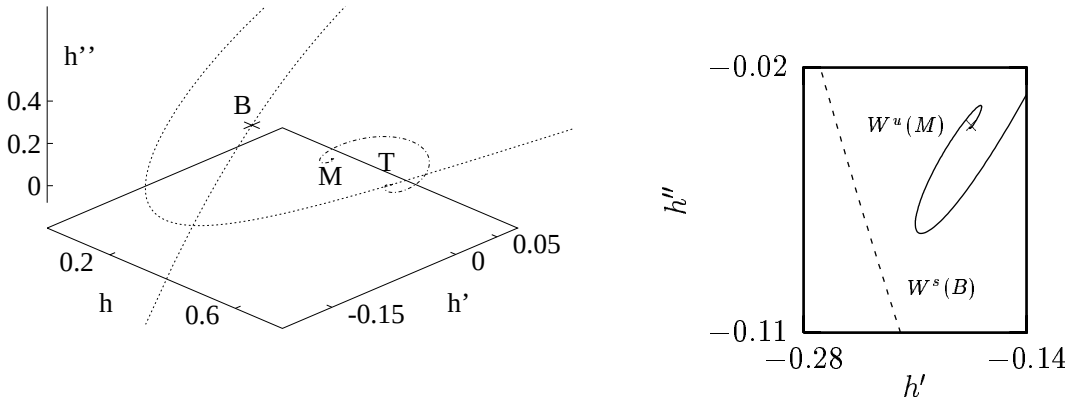

(a) Perspective view (b) Poincaré section P

Fig. 15. Phase portrait for $h_- = 0.355$: In (b) we see that $W^s(B)$ and $W^u(M)$ are well apart, suggesting that no connection from M to T, i.e. no traveling wave solution of (29), exists.

5.2 Stability of the capillary shock profiles

The next question relates to the stability of the capillary shock profiles as traveling wave solutions of the underlying PDE (29). We explore this question numerically. Though every connection of M to T in the three-dimensional phase space of the ODE (36) corresponds to a traveling wave solution of (29), not all of these are *stable* solutions of the PDE. In the stable case, small perturbations of the profile decay with time, whereas for unsta-

ble traveling waves, the perturbed solution is observed to evolve into either a different traveling wave or a double shock solution as described in Section 4.

We determine the stability of a capillary shock profile obtained from the ODE (36) by using it as initial data for the PDE (29), which we then solve using the same numerical procedure as in section 4. Although numerical and interpolation errors supply sufficient perturbations of the profile, we also investigate what happens with the unstable traveling waves if we explicitly apply a small perturbation (height between 0.01 and 0.025) with compact support centered at the maximum of the initial profile. We discuss the results of this investigation for each range of h_- identified in the previous subsection.

In **Case 1**: $h_- < h_1$, we find that the unique traveling wave is stable. Stability is indicated in the Poincaré section of Fig. 10(b) for $h_- = 0.3$, by labeling the intersection point in P with a circle.

For **Case 2:** $h_1 < h_- < h_2$, we distinguish between the two subcases $h_- \leq h_*$ and $h_- > h_*$.

Case 2a: $h_1 < h_- \leq h_*$.

We label the capillary shock profiles according to their place along the spiral curve $W^u(M) \cap P$, using circles and boxes at the intersection points with $W^s(B) \cap P$ to indicate stable and unstable traveling waves, respectively. The stability properties alternate, with a stable traveling wave farthest away from the center $W^u(T) \cap P$ of the spiral. We find numerically that the unstable traveling waves evolve into either the preceding or the following traveling wave, both of which are stable. Specifically, the application of a small negative/positive perturbation selects the preceding/following traveling wave, respectively. These findings are illustrated in the Poincaré sections of Fig. 11(b), for $h_- = 0.33$, and in Fig. 12(b), for $h_- = h_*$.

Case 2b: $h_* < h_- \leq h_2$.

Again, stable and unstable capillary shock profiles alternate, starting with a stable traveling wave farthest away from $W^u(T) \cap P$. Since we now have an even number of capillary shock profiles, the last one is unstable. It decays into the preceding traveling wave if perturbed negatively, and into the double shock profile for positive perturbations. We remark that in Case 2a, such a double shock profile cannot persist, since the Lax shock would have to travel at a higher speed than the undercompressive shock. Fig. 14(b) shows the Poincaré section for this case, with $h_- = 0.333$.

As another example for Case 2b, we show the results for $h_- = 0.3323$. We remind the reader that in Section 4, the long-time solutions of the PDE were computed for these parameter values, i.e., $b = h_+ = 0.1$ and $h_\infty = h_- = 0.3323$, and that, depending on the shape of the initial data (30), (31) and (32), either one of two capillary shock profiles in Fig. 5 or the double shock profile Fig. 6 emerged. As one might expect, the two capillary profiles are those solutions of the ODE which are stable solutions of the PDE. Besides

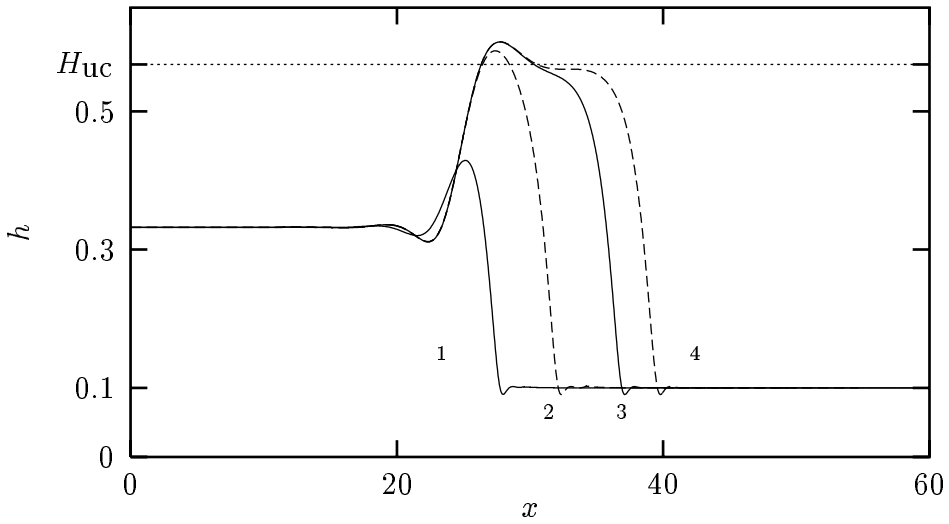

Fig. 16. $h_- = 0.3323$: The stable (—) and unstable (- - -) capillary shock profiles.

these, two more traveling waves are found as solutions of the ODE, which are unstable and hence do not appear as long-time solutions of the PDE.

All four traveling waves are shown in Figs. 16 and 17, where the solid/dashed lines distinguish the stable and unstable profiles. The Poincaré section shows that this is the complete set of capillary shock profiles for $h_- = 0.3323$, $h_+ = 0.1$. The numbers refer to the order in which the capillary shock profiles appear on the spiral formed by $W^u(M)$. For negative perturbations, the (unstable) second and fourth capillary shock profile decay into the first and third, respectively. For positive perturbations, the solutions tend towards the third capillary shock profile or the double shock profile, respectively.

We end this section with a summary of our numerical investigation of the phase space of the ODE (36) and of the stability of the capillary shock profiles as solutions of the PDE (29). We find that, as $h_- < h_*$ increases, $W^s(B)$ moves through the spiral structure of $W^u(M)$, and new capillary shock profiles emerge each time a new turn of the spiral is crossed. More precisely, at each crossing, a new capillary shock profile appears, which then separates into a pair of traveling waves, one stable and the other unstable, suggesting a saddle-node type of bifurcation. The cascade of bifurcations leads to infinitely many traveling wave solutions when $h_- = h_*$, with a heteroclinic orbit from T to B as an accumulation point of the orbits from M to B. The structure of this accumulation point might be investigated rigorously using Sil'nikov's method [21]. Similar behavior is observed as h approaches h_* from above. Furthermore, for $h_- < h_1$, we find a unique and stable capillary shock profile exists; for $h_- > h_2$, there are no capillary shock profiles connecting to h_+. In Section 7 we derive a priori bounds for the left state h_- that a capillary shock profile can connect from as a function of the right state h_+. These bounds are shown in Fig. 20 in that section; the graph shows that the upper bound for h_- is only slightly larger than the numerical values of h_{UC} computed from the phase portrait.

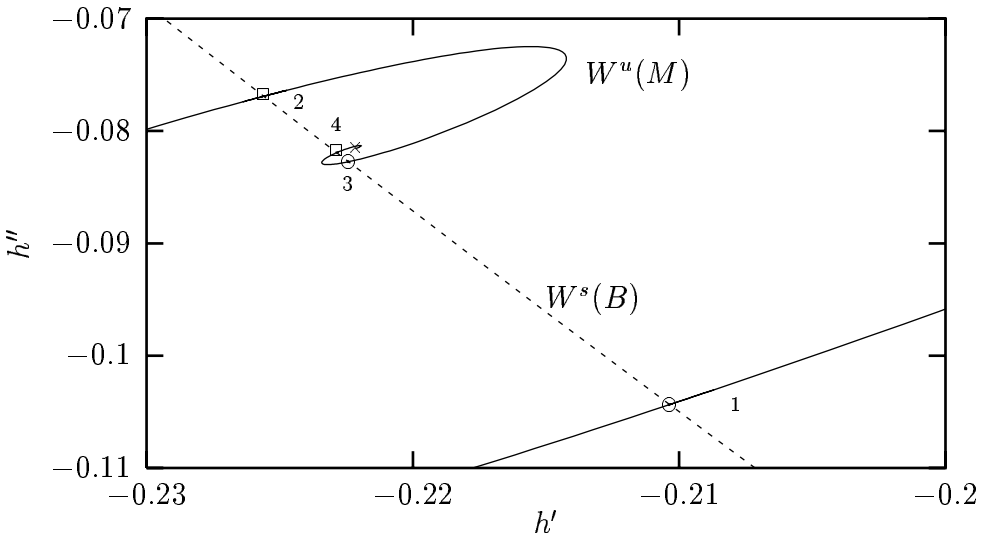

Fig. 17. The Poincaré section P corresponding to Fig. 16; symbols carry over from Fig. 10(b)–14(b).

6 Perturbation analysis for h near $1/3$

In this section, we investigate solutions of (29) near $h = 1/3$. To this end, we rescale parameters and variables using $\delta = \frac{1}{3} - b$, with $0 < \delta \ll 1$. Specifically, we set

$$u_\infty = \delta^{-1}\left(h_\infty - \frac{1}{3}\right), \qquad u = \delta^{-1}\left(h - \frac{1}{3}\right),$$

and introduce rescaled independent variables

$$\xi = 3\delta^{2/3}\left(x - \frac{1}{3}t\right), \qquad \tau = 3\delta^{8/3}t.$$

Then, to leading order in δ, we obtain the equation

$$\boxed{u_\tau - (u^3)_\xi = -u_{\xi\xi\xi\xi},} \tag{40}$$

with boundary conditions at $\xi = \pm\infty$

$$\lim_{\xi\to\infty} u = -1, \qquad \lim_{\xi\to-\infty} u = u_\infty, \qquad \lim_{\xi\to\pm\infty} u_\xi = \lim_{\xi\to\pm\infty} u_{\xi\xi} = 0.$$

Next, we seek traveling wave solutions for (40), which obey

$$\lim_{\xi\to\pm\infty} u = u_\pm, \qquad \lim_{\xi\to\pm\infty} u_\xi = \lim_{\xi\to\pm\infty} u_{\xi\xi} = 0.$$

Substituting $u = u(\eta)$, $\eta = \xi - \sigma\tau$ into (40), and integrating once, we obtain

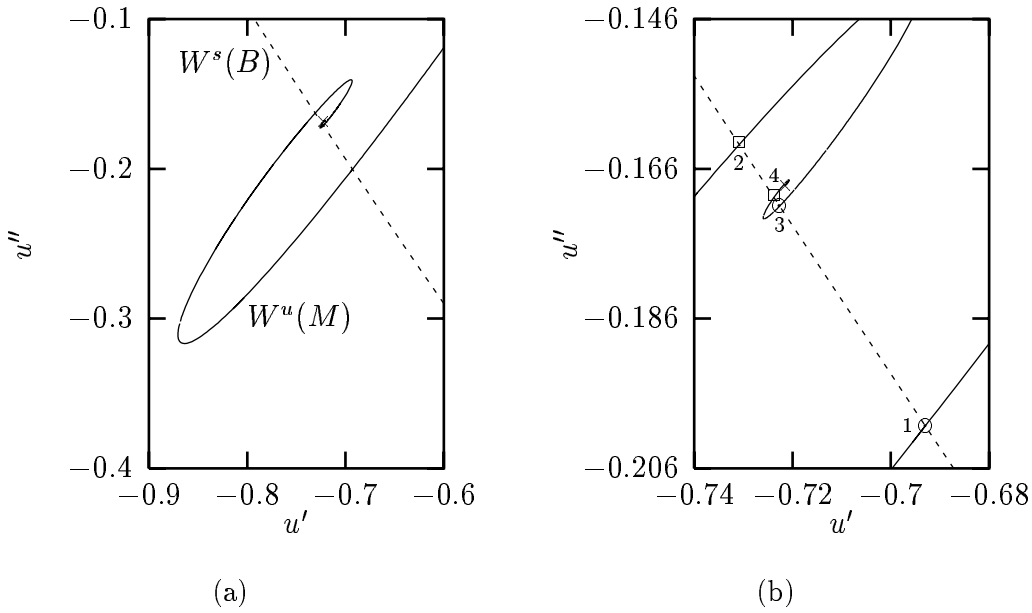

Fig. 18. Sections of the phase portrait of (42) with $P = \{u = (-1 + 2\rho)/3\}$, for $\rho = 0.397$. The enlarged view on the right resolves the four intersection points $W^u(M) \cap W^s(B) \cap P$. Circles and boxes indicate whether they correspond to stable or unstable traveling wave solutions of the PDE (40), respectively.

$$\begin{aligned} \sigma &= -(u_-^2 + u_- u_+ + u_+^2), \\ u_{\eta\eta\eta} &= (u - u_-)(u - u_+)(u + u_- + u_+). \end{aligned} \tag{41}$$

It is convenient to reduce the number of parameters in (42), as follows. When the equilibria u_-, u_+ and $-(u_- + u_+)$ are distinct, an appropriate change of variables in the ODE yields

$$u_{\eta\eta\eta} = (u^2 - 1)(u - \rho). \tag{42}$$

with a single parameter $-1 < \rho < 1$. By symmetry, and bearing in mind the case $u_+ = -1$ corresponding to $h(\infty) = b$, we restrict attention to the range $0 < \rho < 1$.

Equation (42) is equivalent to the first order system

$$u' = v, \qquad v' = w, \qquad w' = (u^2 - 1)(u - \rho),$$

where $' = d/d\xi$. We again have three hyperbolic fixed points, $B = (-1, 0, 0)$, $M = (\rho, 0, 0)$ and $T = (1, 0, 0)$. As for the unscaled equation, B and T have two-dimensional stable manifolds, and M has a one-dimensional stable manifold. To investigate trajectories between equilibria, we study the intersections of stable and unstable manifolds in a Poincaré section with $P = \{u = (-1 + 2\rho)/3\}$. Fig. 18 shows an example for $\rho = 0.397$. We observe that $W^u(M)$ has the same spiral structure around $W^u(T)$ as in equation (35).

As we vary ρ, the relative position of $W^u(M)$ and $W^s(B)$ change, and we have three cases, $\rho < \rho_1 = 0.3793$, where we have a unique connection from M to B, $\rho_1 \le \rho < \rho_2 = 0.4720$, with multiple connections, and $\rho_2 < \rho$, where no connection appears to exist at all. For a special value of $\rho = \rho_* = 0.3959$, we find that T connects to B, which corresponds to the undercompressive part of the double shock solution of (40). In conclusion, the structure of the connecting orbits we are interested in is the same for equation (42) as for the more complicated unscaled equation (35).

For the same example as before, i.e. $\rho = 0.397$, for which the enlarged view of the Poincaré-section in Fig. 18(b) shows that four connections from M to B exist, we investigate the stability of the corresponding traveling wave solutions of the PDE (40). We find the same stability pattern as before, i.e. if we rank the traveling wave solutions according to their position on the spiral of $W^s(M)$, stable and unstable solutions of the PDE (40) alternate. Again, numerical errors were sufficient to initiate the destabilization of the unstable traveling waves, but explicitly applying an initial perturbation showed that the perturbed traveling wave could decay into either of the two neighboring traveling waves, or into the Lax/undercompressive shock combination for the highest ranked traveling wave.

We conclude this section by comparing the numerical results for equation (42) to the computed solutions of (35) for h_+ and h_- close to $1/3$. We do so by using ρ_1, ρ_* and ρ_2 (from equation (42)) to estimate h_1, h_* and h_2, for small δ. For $h_+ = b$, and general h_-, $b < h_- < (1-b)/2$, the corresponding values for $u_\pm$ are

$$u_+ = -1, \qquad u_- = \delta^{-1}\left(h_- - \frac{1}{3}\right).$$

We subsequently transform (41) via

$$\bar{u} = \frac{-2(u-u_+)}{2u_+ + u_-} - 1, \qquad \bar{\xi} = \left(\frac{2u_+ + u_-}{2}\right)^{2/3} \xi,$$

to get (42), after dropping the bars, where ρ is given by the following expression,

$$\rho = \frac{-3u_-}{2u_+ + u_-}.$$

Solving this for h_- yields

$$h_- = \frac{1}{3} - \frac{2\rho}{3+\rho}\left(b - \frac{1}{3}\right),$$

from which we get the following asymptotic estimates by setting $\rho = \rho_1$, ρ_* and ρ_2, respectively,

$$h_1^{\mathrm{as}} = \frac{1}{3} + 0.2245\,\delta, \qquad h_*^{\mathrm{as}} = \frac{1}{3} + 0.2332\,\delta, \qquad h_2^{\mathrm{as}} = \frac{1}{3} + 0.2719\,\delta.$$

Graphical comparison with h_1, h_* and h_2 in Fig. 21 shows good agreement for $0.25 < b < 1/3$.

7 A priori bounds for capillary shock profiles

Recall that a capillary shock profile is a traveling wave solution, $h(x-st)$ of the PDE (10)

$$h_t + (h^2 - h^3)_x = -(h^3 h_{xxx})_x + D(h^3 h_x)_x. \tag{43}$$

Here we derive bounds on the maximum height of any traveling wave solution and also bounds on the admissible far field states $h_\pm$ for such a solution. A traveling wave $h(x-st)$ connecting the state h_- to the state h_+ satisfies

$$-sh_x + (h^2 - h^3)_x = -(h^3 h_{xxx})_x + (Dh^3 h_x)_x \tag{44}$$

where $s = h_- + h_+ - (h_-^2 + h_- h_+ + h_+^2)$ is the speed of the wave. We can integrate (44) once to obtain

$$-sh + (h^2 - h^3) = -h^3 h_{xxx} + Dh^3 h_x + Q \tag{45}$$

where $Q = -h_- h_+ + h_-^2 h_+ + h_+^2 h_-$.

7.1 Bounds for the maximum and minimum height of a traveling wave

As in the proof of Theorem 1, Section 3, (45) has a Lyapunov function

$$L(h) = h_{xx} h_x + R(h)$$

where

$$R'(h) = -\frac{s}{h^2} + \frac{1}{h} - 1 - \frac{Q}{h^3}$$

so that

$$(L(h))_x = (h_{xx})^2 + D(h_x)^2.$$

Unlike in Theorem 1 where we had a convex flux, the function R can have three extrema. When $h_- + h_+ < 1$, the chord connecting these two points on the graph of the flux function intersections the flux at a third value $1 - h_- - h_+$. In such a case, the three extrema are h_-, h_+, and $1 - h_- - h_+$. An example of such a R is shown in Fig. (19).

Although the Conley index argument in the proof of Thm. 1 does not carry over to the case of a non-convex flux, the part of the proof addressing a priori pointwise upper and lower bounds can be extended. In particular, for any traveling wave solution connecting the states h_- and h_+, there exists a priori upper and lower bounds for the extrema of the traveling wave. For example, when $h_+ < h_- < 1 - h_+ - h_-$, the extrema of the traveling wave satisfy

$$h_* < h_{extrema} < h_{**}$$

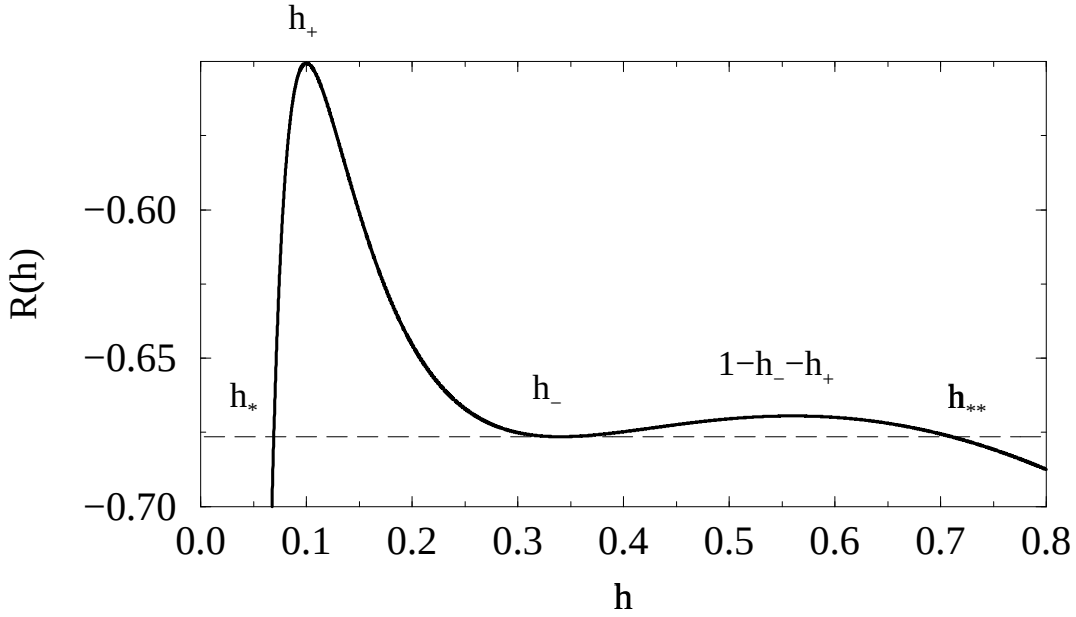

Fig. 19. The function R in the Lyapunov function for the case with gravity and surface tension. Note that the function R decreases for large h. Pictured are the a priori upper and lower bounds h_{**} and h_* for a traveling wave solution connecting the states h_- and h_+.

where h_* and h_{**} are defined by (see Fig. 19)

$$h_* = \min_h\{R(h) > R(h_+)\}, \quad h_{**} = \max_h\{R(h) > R(h_+)\}.$$

7.2 Entropy-flux pairs and constraints on admissible capillary shock profiles

Another related question is to determine which states h_- and h_+ admit a traveling wave solution of (45). Here we show that it is possible to use the concept of entropy-flux pairs to derive a priori bounds for admissible capillary shocks. Any scalar conservation law of the form

$$h_t + (f(h))_x = 0$$

can be rewritten in the form

$$G(h)_t + F(h)_x = 0$$

where G, F are called an entropy-flux pair. Note that G and F are related by $F'(h) = G'(h)f'(h)$. We apply this idea to the traveling wave ODE (45).

First we review how to do this for the case of linear second order diffusion. We consider

$$h_t + (f(h))_x = \epsilon h_{xx}$$

and we want to know what traveling wave solutions exist connecting the left state h_- to the right state $h_+ < h_-$. Let us assume that $h_+ > 0$. If we have such a solution $h(x - st)$

it must satisfy

$$-sh_x + (f(h))_x = \epsilon h_{xx} \tag{46}$$

Now let us consider a function of h, $G(h)$, that satisfies $G''(h) > 0$ on the range of h. Multiplying (46) by $G'(h)$, integrating from $-\infty$ to ∞, and integrating by parts gives

$$-s[G(h)] + [F(h)] = -\epsilon \int G''(h) h_x^2. \tag{47}$$

Here $[A] = A(\infty) - A(-\infty)$. Equation (47) gives us the inequality

$$-s[G(h)] + [F(h)] \leq 0 \tag{48}$$

which is the key equation used to derive bounds on s.

We begin by noting that the case $G'(h) = 1$ gives the shock speed if such a shock exists:

$$s = \frac{f(h_-) - f(h_+)}{h_- - h_+} \tag{49}$$

Now consider the case $G(h) = h^m/m$ for large positive m. Then $G(h_-) > G(h_+)$ so that $[G(h)]$ is negative and (48) yields the result that

$$s \leq \frac{F(h_-) - F(h_+)}{G(h_-) - G(h_+)}.$$

Notice that

$$F(h_-) - F(h_+) = \int_{h_+}^{h_-} f'(h)G'(h)dh = f'(h_-)G(h_-) - f'(h_+)G(h_+) - \int_{h_+}^{h_-} f''(h)G(h)dh$$

so that

$$s \leq \frac{f'(h_-)G(h_-) - f'(h_+)G(h_+)}{G(h_-) - G(h_+)} - \frac{\int_{h_+}^{h_-} f''(h)G(h)dh}{G(h_-) - G(h_+)}.$$

The first term on the right hand side is

$$\frac{f'(h_-) - f'(h_+)G(h_+)/G(h_-)}{1 - G(h_+)/G(h_-)}.$$

Since $G(h_+)/G(h_-) \to 0$ as $m \to \infty$, we see that as $m \to \infty$ the first term goes to $f'(h_-)$. Likewise, the second term goes to zero as $m \to \infty$. To see this, note that

$$\begin{aligned} \| \int_{h_+}^{h_-} f''(h)(G(h)/G(h_-))dh \| &\leq C \int_b^{h_-} (h/h_-)^m dh \\ &= \frac{C}{m+1}(1 - (b/h_-)^{m+1}) \to 0 \quad as \quad m \to \infty. \end{aligned} \tag{50}$$

The upshot is that taking $m \to \infty$ gives the right hand side of the classical Lax entropy condition

$$s \leq f'(h_-). \tag{51}$$

Repeating the above argument for negative m and taking $m \to -\infty$ gives the left hand side of the Lax entropy condition

$$f'(h_+) \leq s. \tag{52}$$

For a non-convex flux function with a single inflection point, a capillary shock profile is admissible if and only if it satisfies the two conditions (51-52).

For the problem with fourth order diffusion, we will not be able to show that all convex entropy functions $G(h)$ yield such inequalities. Instead, we will have a restricted class of entropies for which such conditions hold.

To make this work, we appeal to some previous work on dissipative entropies for fourth order degenerate diffusion (see [2,6,8]). Consider the class of equations

$$-sh_x + (f(h))_x = -\epsilon(h^n h_{xxx})_x, \tag{53}$$

with $n > 0$ and solution $h > 0$. We again ask what restriction the equation imposes on solutions that connect the state h_- at $x \to -\infty$ to the state h_+ at $x \to \infty$. Again, we consider a convex entropy function $G(h)$ such that $G''(h)$ is nonnegative on the range of h. Multiplying equation (53) by $G'(h)$ and integrating by parts gives

$$-s[G(h)] + [F(h)] = \epsilon \int G''(h) h^n h_{xxx} h_x. \tag{54}$$

We can derive an inequality similar to (48) provided that we can find a convex function $G(h)$ such that the right hand side of (54) has a non-positive sign. Following the analysis in [8] and later used in [2,6] to prove results about weak solutions to fourth order degenerate diffusion equations, we see that for $G''(h) = h^{p-n}$, the right hand side of (54) is non-positive whenever $-\frac{1}{2} < p \leq 1$. This gives us a range of power-law entropies and corresponding inequalities

$$-s[G(h)] + [F(h)] \leq 0. \tag{55}$$

We now consider the case $n = 3$. We expect that the bounds given by the entropy will include values of h_- in the set $[0, h_2] \cup h_{UC}$ determined numerically in Sections 4 and 5. The case $p = 1$, with $G(h) = -\log h$, above gives us the sharpest constraint. The bound (55) becomes

$$h_- + h_+ - (h_-^2 + h_- h_+ + h_+^2) \geq \frac{3h_-^2/2 - 2h_- - 3h_+^2/2 + 2h_+}{-\log(h_-) + \log(h_+)}. \tag{56}$$

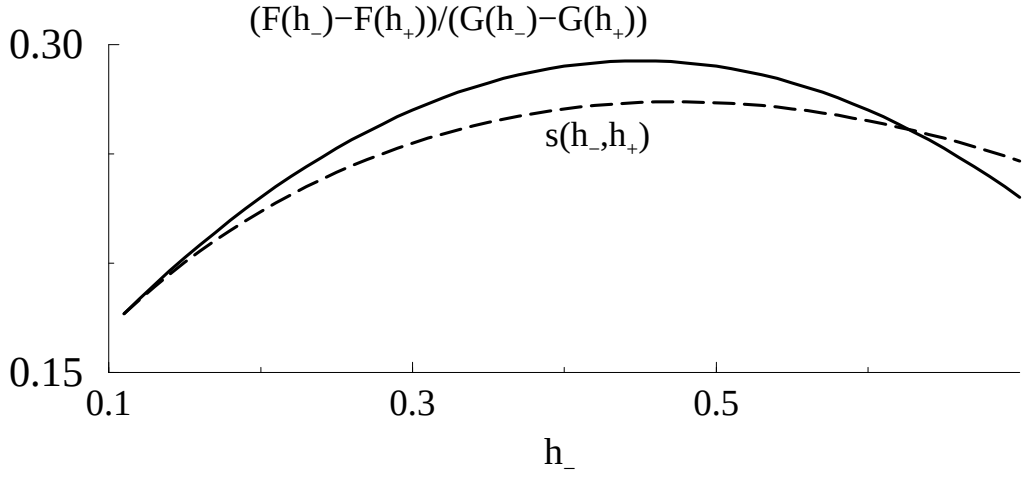

Fig. 20. Graphs of the left and right hand side of equation (56) for fixed $h_+ = 0.1$ as a function of h_-. The graph shows that for $h_+ = 0.1$ the entropy bound restricts admissible connections from $h_+ = 0.1$ to lie in the range $h_+ = 0.1 \leq h_- \leq 0.627$.

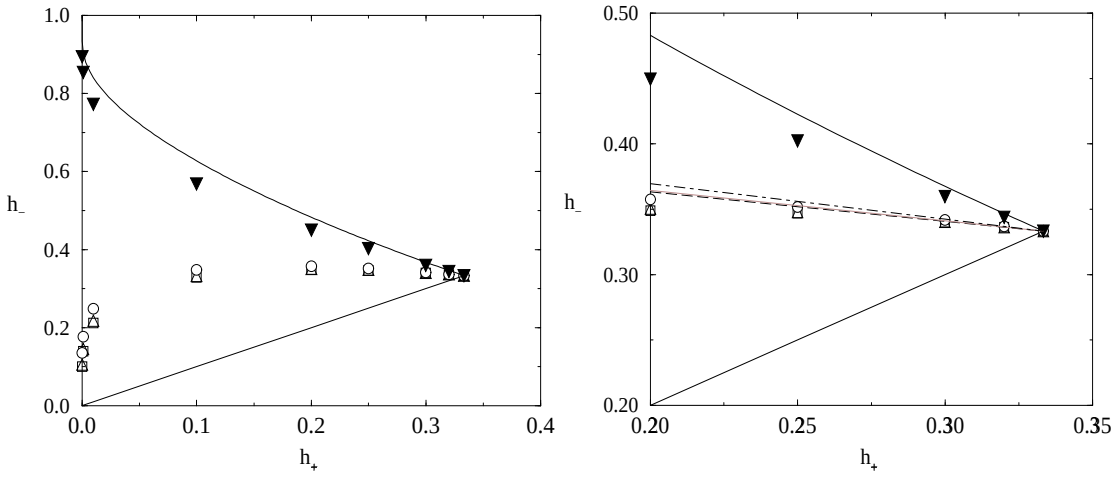

Fig. 21. The upper and lower bounds, shown as solid lines, on h_-, as determined by the entropy $G(h) = -log(h)$, for various values of h_+. We compare these bounds with the numerical values for the undercompressive shock value h_{UC} (dark triangles) and the thresholds h_1 (squares), h_2 (circles) as well as h_* (light triangles). The figure on the right shows a closeup near $h_+ = 1/3$. We compare with the asymptotic theory of Section 6, shown by dashed (h_1), grey (h_*) , and dot-dashed (h_2) lines.

The left and right hand sides of this inequality are shown in Fig. 20. This bound implies that given h_+ there are maximum and minimum values of h_- for which traveling waves exist. These bounds are displayed graphically in Fig. 21.

Fig. 21 compares the bounds on h_- for $0 < h_+ < 1/3$ with the numerical values of $h_{UC}(h_+)$ (dark triangles) of the undercompressive connection and with the value $h_2(h_+)$ (circles) above which classical shocks are no longer observed. Also the values for h_* and h_1 are shown as squares and light triangles; these values are extremely close to each other. Figure 21b shows a close up near $h_+ = 1/3$ and compares with the values predicted by the asymptotic theory in Section 6. Note that the upper bound given by the theory is not much larger than the numerical value for h_{uc}.

8 Concluding remarks

In this paper, we have investigated solutions of the nonlinear partial differential equation (29) that has a non-convex flux and nonlinear fourth order diffusion. The numerical investigation has uncovered a variety of phenomena associated with traveling wave solutions of the equation. These phenomena also occur in the simpler equation (40) with linear fourth order diffusion. The numerics shows that for shock dynamics, the $\epsilon \to 0$ limit of (2) has different behavior from the classical results for the $\epsilon = 0$ hyperbolic conservation law. In particular, initial data corresponding to strong Lax shocks can give rise to a double wave structure that includes an undercompressive shock as the leading front. It is especially interesting that such dynamics results from a purely diffusive (albeit fourth order) regularization of the PDE. Since the double wave structure has a leading shock that is often much larger than the jump for the Lax shock, this is a striking example of how fourth order diffusion can violate the maximum principle. Also along these lines, in the numerical studies of the undercompressive shock, we note that the shock height h_{uc} increases as the downstream film thickness b decreases. The rigorous bound in Section 7 shows that $h_{uc} < 1$ while the numerics shows that h_{uc} is as large as 0.9 for b on the order of 10^{-4}. We conjecture that $h_{uc} \to 1$ as $b \to 0$. If true, this has some interesting consequences for the dynamics of the PDE (29) with jump initial data. In particular, for very small b, with the exception of very small values of h_∞, any h_∞ less than h_{uc} will yield a solution to the PDE that evolves as a double shock structure. Moreover, the leading undercompressive shock will travel at very small speeds: note that if $h_{uc} \to 1$ as $b \to 0$, then s_*, the speed of the undercompressive shock, goes to zero. Moreover, there will be a wide range of $h_\infty < 2/3$ for which the trailing Lax shock actually travels backwards! This is extremely unusual as the characteristics for $h < 2/3$ always travel forwards. We note that this is a different singular behavior from the $b \to 0$ limit when the flux function is convex, e.g. $f(h) = h^2$ or h^3. In these cases, as $b \to 0$, the Lax shock speed approaches a bounded constant determined by h_∞, but the shape of the capillary Lax shock becomes singular. This size of the bump becomes unbounded as $b \to 0$.

Since these are scalar equations in one space dimension and time, the analysis of the

phenomena will be simpler than for a system or with more space dimensions. In particular, the phase portraits uncovered in Section 5 might be established quite easily, including the existence of parameter values for which the vector field has a separatrix corresponding to an undercompressive shock. The proof of stability of the corresponding traveling wave to small perturbations in one dimension might be quite difficult, but there are now a variety of methods for attacking such a problem. A recent paper of Engelberg [15] establishes the stability of weak compressive capillary shock profiles (given by Theorem 2). The stability of the undercompressive viscous-dispersive profile described in [29] is proved in [13], based on the Evans function to study the spectrum of the linearized equation, a technique that has proved effective in other contexts [31,32], including the stability of undercompressive viscous profiles [18]. The stability of undercompressive viscous profiles has also been established for certain systems of equations using a combination of properties of the linearized viscous equation, the hyperbolic equation, and the nonlinearity [38].

In Sections 4 and 5 we discuss stability of the traveling waves as solutions of the PDE (29). Our numerical evidence indicates that when multiple traveling waves exist connecting the far field states h_- and h_+, some of these waves are stable and others are not. On the Poincaré-sections pictured in Section 5, the stable and unstable waves occur as alternating points along the spiral representing the intersection of the unstable manifold from h_- with the Poincaré plane. These stability results are consistent with the idea that a saddle-node bifurcation occurs whenever more traveling waves emerge as h_- is varied (while keeping h_+ fixed). At the center of the spiral is the connection from h_- to the state $1 - h_- - h_+$. When the stable manifold from h_+ intersects this point, we have a heteroclinic connection from the top state $1 - h_- - h_+$ to the bottom state h_+ which takes the form of an undercompressive capillary shock. This shock, although it is the limiting solution of an infinite family of alternating stable and unstable Lax shocks connecting h_- to h_+, appears to be quite stable as a solution of the PDE (29). It would be interesting to try to understand better the relationship of the stability of the infinite family of Lax shocks to the stability of the undercompressive shock. In addition, a very relevant stability question related to the dynamics of driven contact lines in thin films, is whether the traveling waves are stable as solutions of the 2D equation

$$h_t + (f(h))_x = -\nabla \cdot (h^3 \nabla \Delta h)$$

describing the effects of transverse perturbations of the film. The capillary shocks that arise for convex fluxes of the form $f(h) = h^2$ [33] or $f(h) = h^3$ [3,46], are always linearly unstable with respect to perturbations in the transverse variable. This instability is believed to play a role in fingering of a driven contact line (as in paint dripping down a wall). For the case of the non-convex flux considered here (e.g. (29)), recent results [4] indicate that while the capillary Lax shocks are linearly unstable to transverse perturbations, the undercompressive shock is stable. This is believed to be play a role in recent experimental results [17] in which the contact line is much more stable for intermediate film thicknesses.

In this paper, we have investigated new phenomena only for purely fourth order diffusion.

When second order diffusion is included, with D positive but small in equation (10), then we expect the results to be unchanged, as this is a lower order perturbation that will modify the vector field in a benign way. However, as D increases, the undercompressive shocks must become less important as the compressive waves establish themselves, since in the limit $D \to \infty$, as in Subsection 3.1, there are no undercompressive traveling waves. It would be interesting to understand this transition, and whether it takes place at a finite value of D. Our preliminary computations with positive D indicate that for small D the situation is very much like the case $D = 0$ that we consider here. In [3], it was shown that for the convex flux $f(h) = h^3$ (gravity driven films), for each b, there is a critical D above which the capillary ridge, or bump in the shock profile disappears. The disappearance of the bump was related to the change in linearly stability of the front with respect to 2D perturbations. If there is a critical finite D above which undercompressive shocks no longer exist, it would be interesting to know its relationship to the 2D stability problem.

Finally we note that we have used a precursor model for the study of driven contact lines. Many other such models exist, including the slip models [20,22] in which degenerate fourth order diffusion plays a role [6,7]. There are also models that include long range van der Waals interactions [12] involving second order super-diffusive terms [5].

Acknowledgements

We thank Xavier Fanton and Anne Marie Cazabat for correspondences regarding the dynamics of thermally and gravitationally driven films that lead to our initial interest in the mathematical properties of the equations. We thank Andrew Bernoff, Michael Brenner, David Schaeffer, Steve Schecter, John Trangenstein, and Stephanos Venakides for useful conversations.

AB and AM are supported by the Office of Naval research via a PECASE award and by the Sloan foundation. MS is supported by the Army Research Office through grant number DAAG55-98-10128. AB is also a member of the Center for Nonlinear Dynamics and Complex Systems and the Department of Physics at Duke University. MS is an Adjunct Professor at the Dept. of Mathematics at Duke University, where this work was carried out.

References

[1] R. Abeyaratne and J.K. Knowles. Implications of viscosity and strain gradient effects for the kinetics of propagating phase boundaries in solids. *SIAM J. Appl. Math.*, 51:1205–1221, 1991.

[2] Elena Beretta, Michiel Berstch, and Roberta Dal Passo. Nonnegative solutions of a fourth order nonlinear degenerate parabolic equation. *Arch. Rational Mech. Anal.*, 129:175–200,

1995.

[3] A. L. Bertozzi and M. P. Brenner. Linear stability and transient growth in driven contact lines. *Phys. Fluids*, 9(3):530–539, March 1997.

[4] A. L. Bertozzi, A. Münch, X. Fanton, and A. M. Cazabat. Contact line stability and 'undercompressive shocks' in driven thin film flow, 1998.

[5] A. L. Bertozzi and M. Pugh. The lubrication approximation for thin viscous films: the moving contact line with a 'porous media' cut off of Van der Waals interactions. *Nonlinearity*, 7:1535–1564, 1994.

[6] A.L. Bertozzi and M. Pugh. The lubrication approximation for thin viscous films: regularity and long time behavior of weak solutions. *Comm. Pur. Appl. Math.*, 49(2):85–123, February 1996.

[7] Andrea L. Bertozzi. The mathematics of moving contact lines in thin liquid films. *Notices of the American Math. Soc.*, 45(6):698–697, 1998.

[8] Andrea L. Bertozzi, Michael P. Brenner, Todd F. Dupont, and Leo P. Kadanoff. Singularities and similarities in interface flow. In L. Sirovich, editor, *Trends and Perspectives in Applied Mathematics*, volume 100 of *Applied Mathematical Sciences*, pages 155–208. Springer–Verlag, New York, 1994.

[9] Phillippe Carles and Anne-Marie Cazabat. The thickness of surface-tension-gradient-driven spreading films. *J. Coll. Interfac. Sci.*, 157:196–201, 1993.

[10] A. M. Cazabat, F. Heslot, S. M. Troian, and P. Carles. Finger instability of this spreading films driven by temperature gradients. *Nature*, 346(6287):824–826, August 1990.

[11] John R. de Bruyn. Growth of fingers at a driven three–phase contact line. *Phys. Rev. A*, 46(8):R4500–R4503, October 1992.

[12] P.G. de Gennes. Wetting: Statics and dynamics. *Rev. Mod. Phys.*, 57:827, 1985.

[13] J.J. Dodd. *Convective stability of shock profile solutions of a modified KdV-Burgers equation.* PhD thesis, Univ. Maryland, 1996.

[14] E. B. Dussan V and S. Davis. On the motion of a fluid–fluid interface along a solid surface. *J. Fluid Mech.*, 65:71–95, 1974.

[15] Shlomo Engelberg. The stability of the viscous shock profiles of the Burgers equation with a fourth order viscosity. *Commun. in Partial Differential Equations*, 21(5&6):889–992, 1996.

[16] X. Fanton, A. M. Cazabat, and D. Quéré. Thickness and shape of films driven by a Marangoni flow. *Langmuir*, 12(24):5875–5880, 1996.

[17] Xavier Fanton. *Etalement et instabilités de films de mouillage en presence de gradients de tension superficielle.* PhD thesis, Université Paris 6 Pierre et Marie Curie, Paris, 1998.

[18] R. A. Gardner and K. Zumbrun. The gap lemma and geometric criteria for stability of viscous shock profiles. *Comm. Pure Appl. Math.*, 51:789–847, 1998.

[19] Jonathan Goodman and Andrew Majda. The validity of the modified equation for nonlinear shock waves. *J. Comp. Phys.*, 58:336–348, 1985.

[20] H. P. Greenspan. On the motion of a small viscous droplet that wets a surface. *J. Fluid Mech.*, 84:125–143, 1978.

[21] John Guckenheimer and Philip Holmes. *Nonlinear Oscillations, Dynamical Systems, and Bifurcations of Vector Fields.* Springer–Verlag, Berlin, 1986. second printing.

[22] Patrick J. Haley and Michael J. Miksis. The effect of the contact line on droplet spreading. *J. Fluid Mech.*, 223:57–81, 1991.

[23] B. Hayes and M. Shearer. Undercompressive shocks for scalar conservation laws with non-convex fluxes. *Proc. A Royal Soc. Edinburgh*, 1998. to appear.

[24] B.T. Hayes and P.G. LeFloch. Nonclassical shock waves: scalar conservation laws. *Arch. Rat. Mech. Anal.*, 139:1–56, 1997.

[25] Alan C. Hindmarsh. Odepack, a systematized collection of ode solvers. In R. S. Stepleman et al., editor, *Scientific computing*, pages 55–64. North-Holland, Amsterdam, 1983.

[26] Chun Huh and L. E. Scriven. Hydrodynamic model of steady movement of a solid /liquid/fluid contact line. *J. Colloid Interface Sci.*, 35:85–101, 1971.

[27] H. Huppert. Flow and instability of a viscous current down a slope. *Nature*, 300:427–429, 1982.

[28] E. Isaacson, D. Marchesin, and B. Plohr. Transitional waves for conservation laws. *SIAM J. Math. Anal.*, 21:837–866, 1990.

[29] Doug Jacobs, Bill McKinney, and Michael Shearer. Travelling wave solutions of the modified Korteweg-deVries-Burgers equation. *J. Diff. Equ.*, 116(2):448–467, March 1995.

[30] M. F. G. Johnson, R. A. Schluter, M. J. Miksis, and S. G. Bankoff, 1998. Northwestern Univ. Applied Math. Technical Report No. 9604.

[31] C.K.R.T. Jones, R.A. Gardner, and T. Kapitula. Stability of travelling waves for nonconvex scalar viscous conservation laws. *Comm. Pure Appl. Math.*, 46:505–526, 1993.

[32] T. Kapitula and B. Sandstede. Stability of bright solitary–wave solutions to perturbed nonlinear Schrodinger equations, 1997.

[33] Dawn E. Kataoka and Sandra M. Troian. A theoretical study of instabilities at the advancing front of thermally driven coating films. *J. Coll. Int. Sci.*, 192:350–362, 1997.

[34] Dawn E. Kataoka and Sandra M. Troian. Stabilizing the advancing front of thermally driven climbing films. *J. Coll. Int. Sci.*, 203:335–344, 1998.

[35] N. Kopell and L. N. Howard. Bifurcations and trajectories joining critical points. *Advances in mathematics*, 18:306–358, 1975.

[36] Peter D. Lax. Hyperbolic systems of conservation laws ii. *Comm. Pure Appl. Math.*, 10:537–566, 1957.

[37] Peter D. Lax. *Hyperbolic systems of conservation laws and the mathematical theory of shock waves*, volume 11 of *CBMS-NSF Regional conference series in applied mathematics.* SIAM, Philadelphia, PA, 1973.

[38] T.-P. Liu and K. Zumbrun. Nonlinear stability of general undercompressive shock waves. *Comm. Math. Phys.*, 174:319–345, 1995.

[39] V. Ludviksson and E. N. Lightfoot. The dynamics of thin liquid films in the presence of surface-tension gradients. *Am. Inst. Chem. Engrs. J.*, 17(5):1166–1173, 1971.

[40] Christopher K. McCord. Uniqueness of connecting orbits in the equation $y^{(3)} = y^2 - 1$. *Journal of mathematical analysis and applications*, 114:584–592, 1986.

[41] Daniel Michelson. Strong viscous shocks for systems of conservation laws with a high order of dissipation. *J. Diff. Eqs.*, 71:246–254, 1988.

[42] Michael Renardy. A singularly perturbed problem related to surfactant spreading on thin films. *Nonlinear Analysis, Theory, Methods, Applications*, 27(3):287–296, 1996.

[43] M. Shearer, D. G. Schaeffer, D. Marchesin, and P. Paes-Leme. Solution of the Riemann problem for a prototype 2 x 2 system of non-strictly hyperbolic conservation laws. *Arch. Rat. Mech. Anal.*, 97:299–320, 1987.

[44] N. Silvi and E.B. Dussan V. On the rewetting of an inclined solid surface by a liquid. *Physics of Fluids*, 28:5–7, 1985.

[45] M. Slemrod. Admissibility criteria for propagating phase boundaries in a van der Waals fluid. *Arch. Rat. Mech. Anal.*, 81:301–315, 1983.

[46] S. M. Troian, E. Herbolzheimer, S. A. Safran, and J. F. Joanny. Fingering instabilities of driven spreading films. *Europhys. Lett.*, 10(1):25–30, September 1989.

[47] C.C. Wu. New theory of MHD shock waves. In M. Shearer, editor, *Viscous Profiles and Numerical Methods for Shock Waves*. SIAM, 1991.